Monthly Notices
of the
ROYAL ASTRONOMICAL SOCIETY

MNRAS **463,** 3531–3555 (2016) doi:10.1093/mnras/stw2125
Advance Access publication 2016 August 24

The nuclear and extended mid-infrared emission of Seyfert galaxies

I. García-Bernete,[1,2]★ C. Ramos Almeida,[1,2]★ J. A. Acosta-Pulido,[1,2]★
A. Alonso-Herrero,[3,4,5] O. González-Martín,[6] A. Hernán-Caballero,[7,8]
M. Pereira-Santaella,[9] N. A. Levenson,[10] C. Packham,[5,11] E. S. Perlman,[12]
K. Ichikawa,[11] P. Esquej[13] and T. Díaz-Santos[14]

[1]*Instituto de Astrofísica de Canarias, Calle Vía Láctea, s/n, E-38205 La Laguna, Tenerife, Spain*
[2]*Departamento de Astrofísica, Universidad de La Laguna, E-38206 La Laguna, Tenerife, Spain*
[3]*Centro de Astrobiología, CSIC-INTA, ESAC Campus, E-28692 Villanueva de la Cañada, Madrid, Spain*
[4]*Department of Physics, University of Oxford, Oxford OX1 3RH, UK*
[5]*Department of Physics and Astronomy, University of Texas at San Antonio, One UTSA Circle, San Antonio, TX 78249, USA*
[6]*Centro de Radioastronomía y Astrofísica (CRyA-UNAM), 3-72 (Xangari), 8701, Morelia, Mexico*
[7]*Instituto de Física de Cantabria, CSIC-Universidad de Cantabria, E-39005 Santander, Spain*
[8]*Departamento de Astrofísica y CC. de la Atmósfera, Facultad de CC. Físicas, Universidad Complutense de Madrid, E-28040 Madrid, Spain*
[9]*Centro de Astrobiología, CSIC-INTA, Ctra de Torrejón a Ajalvir, km 4, E-28850 Torrejón de Ardoz, Madrid, Spain*
[10]*Gemini Observatory, Casilla 603, La Silla, Chile*
[11]*National Astronomical Observatory of Japan, 2-21-1 Osawa, Mitaka, Tokyo 181-8588, Japan*
[12]*Department of Physics and Space Sciences, Florida Institute of Technology, 150 W. University Blvd., Melbourne, FL 32901, USA*
[13]*European Space Astronomy Centre (ESAC)/ESA, E-28691 Villanueva de la Cañada, Madrid, Spain*
[14]*Núcleo de Astronomía de la Facultad de Ingeniería, Universidad Diego Portales, Av. Ejercito Libertador 441, Santiago, Chile*

Accepted 2016 August 22. Received 2016 August 22; in original form 2016 April 1

ABSTRACT

We present subarcsecond resolution mid-infrared (MIR) images obtained with 8–10 m-class ground-based telescopes of a complete volume-limited ($D_L < 40$ Mpc) sample of 24 Seyfert galaxies selected from the *Swift*/Burst Alert Telescope nine month catalogue. We use those MIR images to study the nuclear and circumnuclear emission of the galaxies. Using different methods to classify the MIR morphologies on scales of ∼400 pc, we find that the majority of the galaxies (75–83 per cent) are extended or possibly extended and 17–25 per cent are point-like. This extended emission is compact and it has low surface brightness compared with the nuclear emission, and it represents, on average, ∼30 per cent of the total MIR emission of the galaxies in the sample. We find that the galaxies whose circumnuclear MIR emission is dominated by star formation (SF) show more extended emission (650 ± 700 pc) than active galactic nuclei (AGN)-dominated systems (300 ± 100 pc). In general, the galaxies with point-like MIR morphologies are face-on or moderately inclined ($b/a \sim 0.4$–1.0), and we do not find significant differences between the morphologies of Sy1 and Sy2. We used the nuclear and circumnuclear fluxes to investigate their correlation with different AGN and SF activity indicators. We find that the nuclear MIR emission (the inner ∼70 pc) is strongly correlated with the X-ray emission (the harder the X-rays the better the correlation) and with the [O IV] λ25.89 μm emission line, indicating that it is AGN-dominated. We find the same results, although with more scatter, for the circumnuclear emission, which indicates that the AGN dominates the MIR emission in the inner ∼400 pc of the galaxies, with some contribution from SF.

Key words: techniques: high angular resolution – galaxies: active – galaxies: nuclei – galaxies: photometry – galaxies: Seyfert – infrared: galaxies.

★ E-mail: igarcia@iac.es (IGB); cra@iac.es (CRA); jap@iac.es (JAAP)

1 INTRODUCTION

Active galactic nuclei (AGN) are powered by accretion of material onto supermassive black holes (SMBHs), which release enormous quantities of energy in the form of radiation and/or mechanical outflows to the host galaxy interstellar medium. This feedback is fundamental to the formation and evolution of the host galaxies (Hopkins & Quataert 2010). Seyfert galaxies are intermediate-luminosity AGN, characterized by a bright unresolved nucleus generally hosted by a spiral galaxy (Adams 1977). Seyfert galaxies are classified by the presence of broad lines (type 1) or otherwise (type 2) in the optical spectrum (Khachikian & Weedman 1971, 1974), and these types depend on orientation, according to the unified model (Antonucci 1993). This scheme proposes that there is dust surrounding the active nucleus distributed in a toroidal geometry, which obscures the central engines of type 2, and allows a direct view in the case of type 1 sources. The dusty torus absorbs the AGN radiation and, then, reprocesses it to emerge in the infrared (IR), peaking in the mid-IR (MIR; ∼5–30 μm), according to torus models (e.g. Pier & Krolik 1992; Efstathiou & Rowan-Robinson 1995; Schartmann et al. 2005; Hönig et al. 2006; Nenkova et al. 2008a,b; Stalevski et al. 2012; Siebenmorgen, Heymann & Efstathiou 2015).

MIR observations of the nuclear regions of active galaxies allow to study the emission of dust heated by the AGN, but also by star formation (SF) when present (e.g. Radomski et al. 2003; Packham et al. 2005; Sales et al. 2013; Alonso-Herrero et al. 2014; Esquej et al. 2014; Ramos Almeida et al. 2014; Ruschel-Dutra et al. 2014; García-Bernete et al. 2015). Prominent features in the MIR spectrum of AGN are the 9.7 μm silicate feature, and the polycyclic aromatic hydrocarbon (PAH) emission bands, although the latter can be diluted by the bright AGN continuum (see e.g. Alonso-Herrero et al. 2014; Esquej et al. 2014; Ramos Almeida et al. 2014; García-Bernete et al. 2015). The PAH features are often used as indicators of the star formation rate (SFR) of galaxies (see e.g. Peeters, Spoon & Tielens 2004; Wu et al. 2005; Diamond-Stanic & Rieke 2012; Esquej et al. 2014), together with low ionization potential (IP) MIR emission lines such as [Ne II] λ12.81 μm (Spinoglio & Malkan 1992; Ho & Keto 2007; Pereira-Santaella et al. 2010; Spinoglio et al. 2012).

The unprecedented angular resolution achieved by 8–10 m-class ground-based telescopes in the MIR is crucial to correctly separate the nuclear emission from the foreground galaxy emission. As the MIR-emitting torus is compact ($r < 10$ pc; see e.g. Tristram et al. 2009; Burtscher et al. 2013), this angular resolution is fundamental to isolate its emission from other emitting sources at larger scales, as well as to disentangle the heating source of the diffuse circumnuclear MIR emission. However, our understanding about the dominant heating source of the dust on these physical scales (inner kpc) remains unclear, because of the paucity of ground-based MIR instruments and the limited size of the samples studied to date (Horst et al. 2008; Gandhi et al. 2009; Levenson et al. 2009; Mason et al. 2012; González-Martín et al. 2013). A major step forward was attained with the publication of the subarcsecond MIR imaging atlas of local AGN (Asmus et al. 2014). These authors presented a compilation of subarcsecond MIR imaging for 253 AGN (204 with nuclear component detected), and found that a large fraction of the galaxies present extended MIR morphologies. They also found that the lower angular resolution data are significantly affected by non-AGN emission, and that the subarcsecond resolution MIR fluxes are generally less than half compared to *Spitzer*/InfraRed Spectrograph (IRS) data in a significant fraction of the sample (31 per cent).

The aim of this work is to study for the first time the nuclear and circumnuclear MIR emission of a complete and volume-limited sample of X-ray-selected Seyfert galaxies (see Section 2) to obtain statistically significant results. Therefore, here we used the nine month *Swift*/Burst Alert Telescope (BAT; Tueller et al. 2008) AGN catalogue, which is a very hard X-ray survey (14–195 keV) to select our AGN sample.

The paper is organized as follows. Sections 2 and 3 describe the sample selection and the observations, respectively. The main results on the MIR emission are presented in Section 4. Section 5 describes the MIR morphological analysis, and in Section 6, we study different MIR correlations with AGN and SF indicators. Finally, in Section 7, we summarize the main conclusions of this work.

Throughout this paper, we assumed a cosmology with $H_0 = 73\,\mathrm{km\,s^{-1}\,Mpc^{-1}}$, $\Omega_\mathrm{m} = 0.27$, and $\Omega_\Lambda = 0.73$, and a velocity-field corrected using the Mould et al. (2000) model, which includes the influence of the Virgo cluster, the Great Attractor, and the Shapley supercluster.

2 SAMPLE SELECTION

Previous ultraviolet (UV), optical and IR surveys are often incomplete, since UV and optical surveys are missing obscured sources, and IR surveys introduce a bias against dust-free AGN. A complete sample would be designed to select AGN by an isotropic property, such as the hard X-ray emission, which is commonly used as an isotropic indicator of AGN luminosity (see e.g. Mulchaey et al. 1994; Meléndez et al. 2008a; Diamond-Stanic, Rieke & Rigby 2009; Rigby, Diamond-Stanic & Aniano 2009).

The very hard 14–195 keV band of the *Swift*/BAT catalogue is far less sensitive to the effects of obscuration than optical or softer X-ray wavelengths. Indeed, this AGN catalogue is one of the most complete to date (see e.g. Winter et al. 2009, 2010; Weaver et al. 2010; Ichikawa et al. 2012; Ueda et al. 2015).

The sample studied here consists of 24 Seyfert galaxies selected from the nine month catalogue observed with *Swift*/BAT (Tueller et al. 2008), which is flux-limited in the very hard 14–195 keV X-ray band (153 sources). The *Swift*/BAT sources were selected based on a detection at 4.8σ or higher. Note that this catalogue is sensitive over 80 per cent of the sky to a flux threshold of 3.5×10^{-11} erg cm^{-2} s^{-1} in the 14–195 keV band and covers one-third of the sky near the ecliptic poles at 2.5×10^{-11} erg cm^{-2} s^{-1}.

We chose the nine month catalogue (Tueller et al. 2008) for selecting our sample, since the sources are bright and nearby, and most of them had archival MIR data when we started this work. Since we are interested in the study of the nuclear and circumnuclear emission of Seyfert galaxies, we selected all the Seyfert galaxies in the nine month catalogue with luminosity distances D_L <40 Mpc. Considering the average angular resolution of 8–10 m-class ground-based telescopes (∼0.3 arcsec in the *N* band), this left us with a sample of 24 Seyfert galaxies for which we have a resolution ≤50 pc in the MIR (hereafter, BAT Complete Seyfert sample at D_L <40 Mpc; $\mathrm{BCS_{40}}$ sample). Here we present high angular resolution MIR imaging observations obtained with 8–10 m-class ground-based telescopes of these galaxies (public and proprietary). See Section 3.1 for further details on the subarcsecond resolution observations.

The $\mathrm{BCS_{40}}$ sample sorted by luminosity distance is shown in Table 1. We present the luminosity distance distribution of the sample in the left panel of Fig. 1. Our sample contains 8 Sy1 and 16 Sy2, with the majority of the galaxies in the 20–40 Mpc range

Table 1. BCS_{40} sample sorted by luminosity distance. Right ascension (RA), declination (Dec.), Seyfert type and galaxy inclination (b/a) were taken from the NASA/IPAC Extragalactic Database (NED). The redshift, D_L, and spatial scale were calculated using a cosmology with $H_0 = 73\,km\,s^{-1}\,Mpc^{-1}$, $\Omega_m = 0.27$, $\Omega_\Lambda = 0.73$ and velocity-field corrected using the Mould et al. (2000) model, which includes the influence of the Virgo cluster, the Great Attractor, and the Shapley supercluster. This galaxy is part of the Virgo Cluster (Binggeli, Sandage & Tammann 1985).

Name	RA (J2000)	Dec. (J2000)	Redshift	Luminosity distance (Mpc)	Spatial scale (pc arcsec^{-1})	Seyfert type	*b/a*
NGC 4395	12h25m48.8s	+33d32m49s	0.0009	3.84	19	1.8	0.83
NGC 5128 (CenA)	13h25m27.6s	−43d01m09s	0.0010	4.28	21	2.0	0.78
NGC 4945	13h05m27.5s	−49d28m06s	0.0011	4.36	21	2.0	0.19
NGC 4051	12h03m09.6s	+44d31m53s	0.0031	12.9	62	1.2	0.75
NGC 6300	17h16m59.5s	−62d49m14s	0.0034	14.0	68	2.0	0.67
NGC 4388	12h25m46.7s	+12d39m44s	0.0101	17.0*	82	2.0	0.19
NGC 4138	12h09m29.8s	+43d41m07s	0.0043	17.7	85	1.9	0.65
NGC 4151	12h10m32.6s	+39d24m21s	0.0049	20.0	96	1.5	0.71
NGC 3227	10h23m30.6s	+19d51m54s	0.0050	20.4	98	1.5	0.67
NGC 7314	22h35m46.2s	−26d03m02s	0.0051	20.9	100	1.9	0.46
NGC 1365	03h33m36.4s	−36d08m25s	0.0052	21.5	103	1.8	0.55
NGC 7582	23h18m23.5s	−42d22m14s	0.0054	22.1	106	2.0	0.42
ESO 005-G004	06h05m41.6s	−86d37m55s	0.0058	24.1	116	2.0	0.21
NGC 7213	22h09m16.3s	−47d10m00s	0.0061	25.1	120	1.5	0.90
NGC 6814	19h42n40.6s	−10d19m25s	0.0062	25.8	123	1.5	0.93
MCG-06-30-015	13h35m53.7s	−34d17m44s	0.0065	26.8	128	1.2	0.60
NGC 5506	14h13m14.9s	−03d12m27s	0.0073	30.1	144	1.9	0.24
UGC 6728	11h45m16.0s	+79d40m53s	0.0078	32.1	153	1.2	0.63
NGC 2110	05h52m11.4s	−07d27m22s	0.0078	32.4	155	2.0	0.76
NGC 2992	09h45m42.0s	−14d19m35s	0.0083	34.4	164	1.9	0.31
NGC 3081	09h59m29.5s	−22d49m35s	0.0083	34.5	164	2.0	0.76
MCG-05-23-016	09h47m40.1s	−30h56m55s	0.0087	35.8	171	2.0	0.45
NGC 3783	11h39m01.7s	−37d44m19s	0.0088	36.4	173	1.2	0.89
NGC 7172	22h02m01.9s	−31d52m11s	0.0092	37.9	180	2.0	0.56

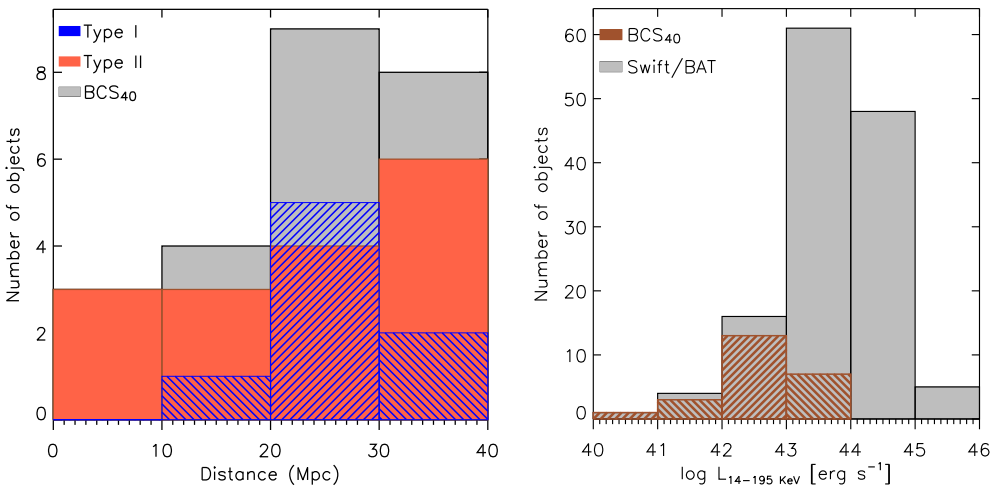

Figure 1. Left panel: luminosity distance distribution of the BCS_{40} sample. The blue hatched and red filled histograms are the distribution of Sy1 and Sy2 galaxies, respectively. The grey filled histograms correspond to the total BCS_{40} sample. Right panel: 14–195 keV X-ray luminosity distribution of the total nine month *Swift*/BAT AGN catalogue (excluding beamed sources – BL Lac objects and blazars) and the BCS_{40} sample (grey filled and brown hatched histograms, respectively).

(71 per cent of the sample). The median distance of the BCS_{40} sample is 24.1 Mpc. Hereafter, the Seyfert types are referred as Sy1 (Seyferts 1, 1.2 and 1.5) and Sy2 (Seyferts 1.8, 1.9 and 2). The closest galaxies in the sample are Sy2, although the median values for Sy1 and Sy2 are relatively similar, 25.8 Mpc and 22.1 Mpc, respectively. In the right panel of Fig. 1, we present the comparison between the nine month *Swift*/BAT catalogue and BCS_{40} sample 14–195 keV X-ray luminosity. The latter corresponds to the lowest luminosity region of the nine month *Swift*/BAT sample.

3 OBSERVATIONS

In this section, we describe all the MIR observations analysed in this work, which we divide in subarcsecond and arcsecond resolution data.

3.1 Subarcsecond resolution data

Here we describe the subarcsecond resolution MIR imaging data, which are from 8–10 m-class ground-based telescopes. For all subarcsecond resolution MIR observations, the standard MIR chopping and nodding technique was used to remove the time-variable sky background and the thermal emission from the telescope. In addition to the target observations, an image of a point spread function (PSF) standard star was obtained immediately after or before the science target for accurately sampling the image quality, and to allow flux calibration.

In Fig. A1 of Appendix A, we present the *N*-band images of the BCS_{40} sample, and Table 2 summarizes the details of the observations, as well as the derived galaxy measurements. In the following, we consider that the nucleus is resolved when the full width at half-maximum (FWHM) of the galaxy is larger than the FWHM of the PSF standard star. In Table 2, we also present the classification of the MIR images of the galaxies by comparing the FWHM of the PSF standard star and the galaxy in each band.

3.1.1 *Gran Telescopio CANARIAS/CanariCam observations*

We obtained MIR images of three Seyfert galaxies (NGC 4388, NGC 3227 and UGC 6728) and their corresponding PSF standard star with the filter Si2 (λ_c = 8.7 μm) using the instrument CanariCam (CC; Telesco et al. 2003) on the 10.4 m Gran Telescopio CANARIAS (GTC). NGC 4388 and NGC 3227 were observed as part of an ESO/GTC large programme (182.B-2005; Alonso-Herrero et al. 2016), and UGC 6728 as part of proposal GTC43-15A (PI: I. García-Bernete). CC is an MIR (7.5–25 μm) imager with spectroscopic, coronagraphic and polarimetric capabilities and uses a Si:As impurity band conduction (IBC) detector, which covers a field of view (FOV) of 26 arcsec × 19 arcsec on the sky and it has a pixel scale of 0.0798 arcsec (hereafter 0.08 arcsec). The chopping and nodding throws were 15 arcsec.

The data reduction was carried out with the REDCAN pipeline (González-Martín et al. 2013), which performs sky subtraction, stacking of individual observation, rejection of the bad frames and flux calibration. The spatial resolution of the image was determined by measuring the FWHM of the PSF standard star. See Table 2 for further details on the observations.

3.1.2 *Gemini/T-ReCS observations*

We retrieved MIR images of 10 Seyfert galaxies and their corresponding PSF standard stars per filter and science object from the Gemini archive. The images were taken with the Si2 (λ_c = 8.7 μm) and Qa (λ_c = 18.3 μm) filters using the instrument Thermal-Region Camera Spectrograph (T-ReCS; Telesco et al. 1998) on the 8.1 m Gemini-South Telescope. T-ReCS is an MIR (8-25 μm) imager and long-slit spectrograph and uses a Raytheon Si:As IBC detector, which covers an FOV of 28.5 arcsec × 21.4 arcsec, providing a pixel scale of 0.089 arcsec. See Table 2 for further details on the observations.

We reduced the Gemini/T-ReCS data using the REDCAN pipeline (González-Martín et al. 2013), as described in Section 3.1.1.

3.1.3 *Gemini/MICHELLE observations*

We compiled data for seven Seyfert galaxies obtained with the instrument MICHELLE (Glasse, Atad-Ettedgui & Harris 1997) on the 8.1 m Gemini-North Telescope. MICHELLE is an MIR (7-26 μm) imager and spectrograph, which uses an Si:As IBC detector, covering an FOV of 32 arcsec × 24 arcsec on the sky. Its pixel scale is 0.1005 arcsec. The images were taken with different filters, namely N′ (λ_c = 11.2 μm), Si5 (λ_c = 11.6 μm), Si6 (λ_c = 12.5 μm) or Qa (λ_c = 18.1 μm). See Table 2 for further details on the observations.

The Gemini/MICHELLE data reduction was carried out with the Gemini IRAF[1] packages, particularly with the MIDIR (Tody 1986) reduction task. The Gemini IRAF packages include sky subtraction, stacking of individual images and rejection of bad images. The flux calibration was carried out using the PHOT IRAF task and the image of the PSF standard star to work out the relation between count and flux.

3.1.4 *Gemini/OSCIR observations*

Two images of the galaxy NGC 4151 were taken with the N (λ_c =10.75 μm) and IHW18 (λ_c =18.17 μm) filters using the University of Florida MIR camera/spectrometer OSCIR on the 8.1 m Gemini-North telescope. OSCIR uses a Rockwell 128 × 128 Si:As IBC detector. On Gemini North, OSCIR has a plate scale of 0.089 arcsec pixel^{-1}, corresponding to an FOV of 11.4 arcsec × 11.4 arcsec. The chopping and nodding throws were 15 arcsec. See Table 2 for further details on the observations.

We took the fully reduced and flux-calibrated images from Radomski et al. (2003), also presented in Ramos Almeida et al. (2009). The data were reduced using in house-developed IDL routines (see Radomski et al. 2003 for further details on the data reduction).

3.1.5 *Very Large Telescope/VISIR observations*

We finally compiled MIR images for the rest of the sample (four Seyfert galaxies) taken with different filters (see Table 2) with the instrument VISIR (Lagage et al. 2004) on the Unit 3 of the 8.2 m Very Large Telescope (VLT) telescope (Melipal). VISIR is an MIR (16.5-24.5 μm) imager and spectrograph, which uses 256 × 256 Si:As IBC detector, covering an FOV of 19.2 arcsec × 19.2 arcsec and its pixel scale is 0.075 arcsec.

We downloaded the fully reduced and calibrated science data of the galaxies from the Subarcsecond mid-infrared atlas of local AGN[2] (Asmus et al. 2014). In addition, we retrieved PSF standard stars for each observation from the ESO archive.[3] We reduced the PSF standard stars with the VISIR[4] pipeline, which performs flat-fielding correction, bad pixel removal, source alignment, and co-addition of frames are executed to produce a combined image for each filter. See Table 2 for further details on the observations.

[1] IRAF is distributed by the National Optical Astronomy Observatory, which is operated by the Association of Universities for Research in Astronomy (AURA) under cooperative agreement with the National Science Foundation.
[2] http://dc.zah.uni-heidelberg.de/sasmirala/q/cone/form
[3] http://archive.eso.org/eso/eso_archive_main.html
[4] http://www.eso.org/observing/dfo/quality/VISIR/pipeline/pipe_gen.html

Table 2. Summary of the ground-based MIR imaging observations. Columns from 1 to 6 list the galaxy name, the central wavelength and filter width (μm), the filter name, the observation date, the telescope/instrument and the on-source exposure time. Columns 7 and 8 correspond to the FWHM and ellipticity of the nucleus of the galaxy. Column 9 lists the standard deviation of the sky background in mJy pixel^{-1} units. Columns 10 and 11 are the same as columns 7 and 8, but for the PSF standard star. Column 12 indicates if the galaxy nucleus is resolved or not. Finally, columns 13–15 correspond to the nuclear fluxes, the corresponding percentages of PSF subtraction used for determining each nuclear flux and the total fluxes. BR corresponds to barely resolved nucleus. Note that † and ‡ correspond to nuclear fluxes calculated using aperture photometry and aperture corrections, when the nucleus is not well defined or the structure of the PSF is not symmetric, respectively.

Name	Wavel. $\lambda_c/\Delta\lambda$ (μm)	Filter name	Observation date	Telescope / instrument	Exposure time (s)	FWHM galaxy (arcsec)	e_{gal}	Stand. dev. (σ)	FWHM PSF (arcsec)	e_{PSF}	Resol. Nuc.	Nuclear flux (mJy)	Best PSF per cent	Total flux (mJy)
NGC 4395	12.5/1.2	Si6	2010/02/05	Gemini/MICHELLE	1011	0.369	–	0.06	0.369	0.03	BR	7	100	9
NGC 5128	8.74/0.78	Si2	2004/05/03	Gemini/T-ReCS	608	0.311	0.07	0.06	0.304	0.05	BR	511	90	611
	18.33/1.5	Qa	2004/05/03	Gemini/T-ReCS	2042	0.442	0.13	0.87	0.533	0.13	×	1473	80	2139
NGC 4945	8.74/0.78	Si2	2006/03/17	Gemini/T-ReCS	261	3.855	0.73	0.08	0.322	0.05	√	47	...†	1241
	18.33/1.5	Qa	2006/03/17	Gemini/T-ReCS	261	–	–	1.17	0.524	1.57	–	78	...†	1765
NGC 4051	11.6/1.1	Si5	2010/02/02	Gemini/MICHELLE	156	0.372	0.07	0.10	0.355	0.07	BR	408	100	438
NGC 6300	8.59/0.84	PAH1	2008/03/22	VLT/VISIR	362	0.320	0.25	0.09	0.246	0.08	√	141	90	292
	10.49/0.32	SIV	2008/03/22	VLT/VISIR	721	0.383	0.23	0.17	0.281	0.15	√	71	70	167
	11.25/1.18	PAH2	2008/03/22	VLT/VISIR	362	0.352	0.21	0.09	0.346	0.09	BR	259	90	347
	13.04/0.44	NeII_2	2008/03/22	VLT/VISIR	361	0.398	0.24	0.31	0.365	0.10	BR	474	90	792
NGC 4388	8.7/1.1	Si2	2015/02/01	GTC/CC	1044	0.366	0.39	0.10	0.380	0.13	×	74	70	108
NGC 4138	11.6/1.1	Si5	2010/02/02	Gemini/MICHELLE	259	0.409	–	0.08	0.355	0.07	√	9	70	12
NGC 4151	10.75/5.2	N	2001/05/07	Gemini/OSCIR	360	0.573	0.13	0.09	0.536	0.06	BR	1452	90	1719
	18.17/1.7	IHW18	2001/05/07	Gemini/OSCIR	480	0.640	0.25	0.63	0.577	0.02	BR	3243	100	4242
NGC 3227	8.7/1.1	Si2	2014/03/17	GTC/CC	627	0.321	0.08	0.08	0.287	0.02	BR	147	80	260
	11.2/2.4	Np	2006/07/04	Gemini/MICHELLE	376	0.401	0.07	0.04	0.424	0.15	×	318	90	436
NGC 7314	8.74/0.78	Si2	2010/08/20	Gemini/T-ReCS	319	0.402	0.11	0.08	0.354	0.07	√	32	80	48
	18.33/1.5	Qa	2010/09/25	Gemini/T-ReCS	811	0.545	0.11	0.25	0.555	0.12	×	122	80	162
NGC 1365	8.74/0.78	Si2	2011/09/08	Gemini/T-ReCS	145	0.391	0.19	0.10	0.322	0.06	√	126	60	1111
	18.33/1.5	Qa	2011/09/08	Gemini/T-ReCS	521	0.579	0.26	0.54	0.554	0.10	BR	435	60	1896
NGC 7582	8.74/0.78	Si2	2011/09/07	Gemini/T-ReCS	296	0.359	0.08	0.07	0.409	0.12	×	208	60	863
	18.33/1.5	Qa	2011/09/07	Gemini/T-ReCS	515	0.692	0.35	0.33	0.513	0.11	√	289	60	2214
ESO 005-G004	8.59/0.84	PAH1	2010/11/13	VLT/VISIR	181	0.536	0.41	0.07	0.255	0.05	√	7	100	16
	11.25/1.18	PAH2	2010/11/22	VLT/VISIR	1994	0.392	0.22	0.04	0.384	0.17	BR	21	90	27
	11.88/0.74	PAH2_2	2010/11/22	VLT/VISIR	1986	0.381	0.37	0.05	0.365	0.13	BR	27	90	38
	13.04/0.44	NeII_2	2007/10/09	VLT/VISIR	181	0.942	–	0.38	0.534	0.16	√	89	60	162
	18.72/1.76	Q2	2010/11/16	VLT/VISIR	497	1.696	–	0.62	0.536	0.29	√	58	30	69
NGC 7213	8.74/0.78	Si2	2010/12/16	Gemini/T-ReCS	145	0.399	0.26	0.12	0.375	0.05	BR	56	90	76
	18.33/1.5	Qa	2007/06/07	Gemini/T-ReCS	319	0.607	0.06	0.74	0.534	0.05	√	224	80	300
NGC 6814	8.74/0.78	Si2	2009/08/28	Gemini/T-ReCS	145	0.284	0.17	0.11	0.280	0.04	BR	42	90	55
	18.33/1.5	Qa	2009/08/28	Gemini/T-ReCS	203	0.627	–	0.98	0.534	0.11	√	107	40	153
MCG-06-30-015	8.59/0.84	PAH1	2010/03/10	VLT/VISIR	362	0.281	0.25	0.27	0.216	0.07	√	121	80	291
	10.49/0.32	SIV	2006/04/14	VLT/VISIR	177	0.314	0.23	0.18	0.296	0.18	BR	308	90	378
	11.25/1.18	PAH2	2006/04/14	VLT/VISIR	181	0.330	0.25	0.14	0.317	0.21	BR	306	80	474
	11.88/0.74	PAH2_2	2010/03/10	VLT/VISIR	362	0.336	0.11	0.35	0.308	0.12	BR	222	70	418
	12.27/0.36	NeII_1	2006/04/14	VLT/VISIR	180	0.350	0.12	0.29	0.336	0.16	BR	304	80	460
NGC 5506	11.2/2.4	Np	2006/04/06	Gemini/MICHELLE	141	0.378	0.04	0.06	0.399	0.12	×	758	80	885
	18.1/1.9	Qa	2006/04/06	Gemini/MICHELLE	109	0.562	0.10	0.63	0.534	0.07	BR	1533	90	2126
UGC 6728	8.7/1.1	Si2	2015/08/01	GTC/CC	695	0.843	-	0.10	0.606	0.21	√	27	...‡	41
NGC 2110	11.2/2.4	Np	2007/03/18	Gemini/MICHELLE	376	0.422	0.06	0.07	0.481	0.10	×	305	80	308
NGC 2992	11.2/2.4	Np	2006/05/12	Gemini/MICHELLE	188	0.372	0.17	0.07	0.325	0.23	√	159	90	347
	18.1/1.9	Qa	2006/05/12	Gemini/MICHELLE	163	0.561	0.22	0.68	0.537	1.67	BR	513	90	647
NGC 3081	8.74/0.78	Si2	2006/01/25	Gemini/T-ReCS	130	0.310	0.23	0.13	0.296	0.15	BR	75	90	99
	18.33/1.5	Qa	2006/01/25	Gemini/T-ReCS	304	0.623	1.11	0.83	0.561	0.16	BR	364	80	613
MCG-05-23-016	8.99/0.28	ArIII	2007/01/30	VLT/VISIR	699	0.265	0.14	0.09	0.293	0.10	×	349	60	472
	11.88/0.74	PAH2_2	2006/03/12	VLT/VISIR	361	0.338	0.08	0.19	0.335	0.15	BR	599	90	752
	17.65/1.66	Q1	2007/01/30	VLT/VISIR	684	0.483	0.13	0.42	0.461	0.10	BR	1168	80	1640
	18.72/1.76	Q2	2015/12/18	VLT/VISIR	855	0.504	0.22	0.37	0.477	0.27	BR	1463	100	1706
NGC 3783	8.74/0.78	Si2	2012/05/01	Gemini/T-ReCS	145	0.312	0.03	0.12	0.295	0.11	BR	248	90	347
	18.33/1.5	Qa	2012/05/05	Gemini/T-ReCS	319	0.521	0.10	0.59	0.532	0.13	×	989	90	1156
NGC 7172	8.74/0.78	Si2	2011/09/20	Gemini/T-ReCS	145	0.409	0.27	0.10	0.389	0.06	BR	59	80	96
	18.33/1.5	Qa	2001/09/20	Gemini/T-ReCS	348	0.540	–	0.59	0.600	0.09	×	117	70	145

3.2 Arcsecond resolution data

Here we describe the arcsecond resolution MIR data, which correspond to observations taken with the *Spitzer Space Telescope* and the *Wide-field Infrared Survey Explorer* (*WISE*; Wright et al. 2010), both with lower spatial resolution but higher sensitivity than the ground-based observations described in Section 3.1.

3.2.1 Spitzer Space Telescope observations

We compiled arcsecond resolution MIR data of 18 galaxies obtained with the instrument Infrared Array Camera (IRAC; Fazio et al. 2004) using the 8 μm channel (angular resolution ∼1.9 arcsec). The IRAC FOV is 5.2 arcmin × 5.5 arcmin on the sky and its pixel scale is 1.2 arcsec. We downloaded the reduced and calibrated mosaiked data from the *Spitzer* Heritage Archive (SHA). Note that these mosaics are re-sampled to a pixel size of 0.6 arcsec. The 8 μm IRAC data are shown in Fig. A2 of Appendix A. Besides, in Fig. A1 of Appendix A, we also show the comparison between the subarcsecond resolution *N*-band data and the arcsecond resolution 8 μm Spitzer images for the nuclear region (≤650 pc) of the galaxies.

In addition, low-resolution MIR spectra were retrieved for the whole sample from the Cornell Atlas of *Spitzer*/IRS Source (CASSIS[5] v4; Lebouteiller et al. 2011). The spectra were obtained using the IRS (Houck et al. 2004). The bulk of the observations were obtained in staring mode using the low-resolution (*R*∼60–120) IRS modules: the short-low (SL; 5.2–14.5 μm) and the long-low (LL; 14–38 μm). The spectra were reduced with the CASSIS software, using the optimal extraction to get the best signal-to-noise ratio. We only needed to apply a small offset to stitch together the different modules, taking the shorter wavelength module (SL2; 5.2–7.6 μm) as the basis, which has associated a slit width of 3.6 arcsec. The spectra are shown in Appendix B. Note that for NGC 4138, there is no low-resolution staring mode spectrum. Therefore, we have extracted a spectrum in a 7.7 arcsec aperture diameter from the spectral mapping observations available in the SHA.

3.2.2 WISE observations

For these galaxies in our sample that do not have IRAC images available and for cases whose IRAC images are saturated, we downloaded MIR images from the *WISE* All-Sky Data Release,[6] taken in the 12 μm band (angular resolution ∼6.5 arcsec). The *WISE* FOV is 47 arcmin × 47 arcmin on the sky and its pixel scale is 2.75 arcsec. We downloaded the reduced fully calibrated data. We show the 12 μm *WISE* images in Fig. A2 of Appendix A. Besides, in Fig. A1 of Appendix A, we also include the arcsecond resolution 12 μm *WISE* images in the comparison between the subarcsecond and arcsecond resolution *N*-band images.

4 MIR EMISSION

In this section, we study in detail the properties of the inner regions (few hundred parsecs) of the BCS_{40} sample.

4.1 Subarcsecond resolution nuclear fluxes: subtraction of scaled PSFs

Taking advantage of the angular resolution provided by the ground-based instruments described in Section 3.1, we obtained nuclear fluxes for all the galaxies in our sample. We used the PSF standard stars to obtain these nuclear fluxes. Fig. 2 shows an example of PSF subtraction at various levels (in ≥3σ contours) for the MIR (λ_c = 10.75 μm) GEMINI/OSCIR image of NGC 4151. The method consists in the following: we first matched the PSF-star image (see top-right panel of Fig. 2) to the peak of the galaxy emission, that is, at a 100 per cent level. Then, we subtracted the scaled PSF-star from the galaxy image (see top-left panel of Fig. 2) at different percentage peak levels until we obtained a non-oversubtracted residual image. This is something that we determine by looking at the 1D profile shown in the bottom-right panel of Fig. 2, but also at the contour plots shown in the middle and bottom-left panels (100, 90 and 80 per cent in the case of Fig. 2). The contour plot at 100 per cent subtraction appears clearly oversubtracted in the galaxy nucleus, and the 1D profile as well. The 90 per cent subtraction is the best fit according to the previous criteria. Finally, we measured the unresolved component by integrating the emission in a 1 arcsec radius aperture[7] on the scaled PSF-star image. The host galaxy contribution corresponds to the total galaxy emission minus the scaled PSF (i.e. the residual of the subtraction). This method has been widely tested in ground-based MIR images (e.g. Soifer et al. 2000; Radomski et al. 2002, 2003; Levenson et al. 2009; Ramos Almeida et al. 2009, 2011b, 2014; Mason et al. 2012; García-Bernete et al. 2015; Martínez-Paredes et al. 2015).

The MIR nuclear fluxes calculated using this method are listed in Table 2. The estimated uncertainty of the fluxes determined using

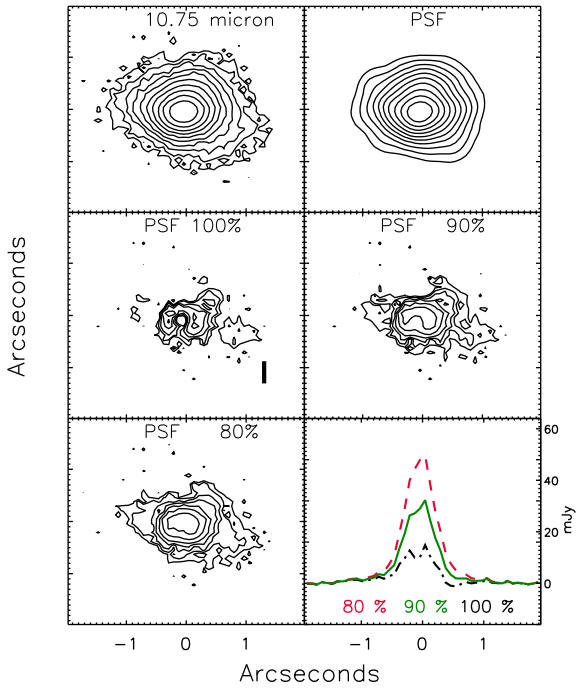

Figure 2. MIR (λ_c =10.75 μm) GEMINI/OSCIR contours at ≥3σ of NGC 4151, the PSF standard star and, scaled PSF subtraction at different levels, and 1D profiles of the residuals at 100, 90 and 80 per cent levels (black dot–dashed, solid green and red dashed lines, respectively). The best subtraction is 90 per cent according to the flat galaxy profile shown in the bottom-right panel. North is up, and east to left.

[5] http://cassis.astro.cornell.edu/atlas/
[6] http://irsa.ipac.caltech.edu/Missions/wise.html
[7] Note that we carried out the sky subtraction using a concentric ring wide enough to contain a good estimate of the sky background.

Table 3. Details on the MIR and X-ray data. The 8 μm nuclear fluxes were calculated by using a 1 μm window centred at 8 μm in the scaled AGN component (see Section 4.1). Column 1 lists the galaxy name. Columns 2–5 correspond to the subarcsecond resolution nuclear fluxes, the arcsecond resolution nuclear fluxes, the best percentage of PSF subtraction used with the arcsecond resolution data and the 12 μm WISE fluxes. Columns 6 and 7 list the intrinsic 2–10 kev X-ray luminosities and their references. Column 8 and 9 correspond to the 14–195 keV X-ray luminosities and the column densities, respectively, taken from the *Swift*/BAT catalogue (Tueller et al. 2008). Finally, columns 10 and 11 list the [Ne II] and [O IV] emission line luminosities and column 12 corresponds to their references. References: (a) Nardini & Risaliti (2011); (b) de Rosa et al. (2012); (c) Vaughan et al. (2011); (d) Liu et al. (2014); (e) Rivers, Markowitz & Rothschild (2011); (f) Brightman & Nandra (2011); (g) Winter et al. (2009); (h) Shu, Yaqoob & Wang (2010); (i) Eguchi et al. (2011); (j) Weaver et al. (2010); (k) Goulding & Alexander (2009); (l) Pereira-Santaella et al. (2010).

Name	$F^{\rm Sub}_{\rm Nuc}$ 8 μm (mJy)	$F^{\rm Arc}_{\rm Nuc}$ 8 μm (mJy)	Best ArcRes per cent subt.	$F_{\rm WISE}$ 12 μm (mJy)	$L_{2-10\,\rm keV}$ (10^{41} erg s^{-1})	2–10 keV Ref.	$L_{14-195\,\rm keV}$ (10^{41} erg s^{-1})	log $N_{\rm H}$ (cm^{-2})	$L_{[\rm Ne\,II]}$ (12.81 μm) (10^{39} erg s^{-1})	$L_{[\rm O\,IV]}$ (28.89 μm) (10^{39} erg s^{-1})	MIR lines Ref.
NGC 4395	2	14	90	11	0.07	a	0.46	22.30	0.08 ± 0.01	0.14 ± 0.01	j
NGC 5128	564	861	IRS	2833	2.45	b	16.40	22.74	4.23	2.88	j
NGC 4945	12	1856	IRS	2831	1.40	b	4.41	24.60	15.90 ± 1.40	1.12 ± 0.30	k
NGC 4051	183	247	80	468	2.36	c	9.16	20.47	3.92 ± 0.18	7.36 ± 0.41	j
NGC 6300	140	285	IRS	467	9.17	b	21.34	23.34	2.70 ± 0.14	6.91 ± 0.53	k
NGC 4388	74	223	70	454	102.40	b	87.48	23.63	25.80 ± 1.60	108.00 ± 9.00	j
NGC 4138	3	12	90	38	1.85	d	7.87	22.90	1.21 ± 0.19	0.76 ± 0.07	j
NGC 4151	746	1005	IRS	1650	1039.00	e	179.00	22.48	64.10	113.00	j
NGC 3227	79	192	60	508	20.49	e	64.23	22.80	32.40 ± 3.40	32.3 ± 1.20	j
NGC 7314	23	47	50	112	36.78	d	29.79	21.79	4.69 ± 0.39	36.40 ± 4.10	j
NGC 1365	84	433	IRS	1942	32.52	f	39.82	23.60	89.40 ± 9.70	80.40 ± 4.90	j
NGC 7582	57	171	IRS	1309	64.84	g	39.15	22.98	147.00 ± 2.00	133.00 ± 1.00	j
ESO 005-G004	5	29	50	167	11.07	g	29.19	23.88	11.60 ± 0.10	3.12 ± 0.13	j
NGC 7213	31	124	60	239	14.47	d	39.20	20.60	20.70 ± 1.00	2.07 ± 0.44	j
NGC 6814	29	79	90	116	26.52	d	49.38	20.76	5.73	21.50	l
MCG-06-30-015	99	134	IRS	334	33.06	h	64.45	21.67	3.61 ± 0.10	20.20 ± 0.10	j
NGC 5506	638	936	IRS	1051	161.10	e	255.80	22.53	99.50 ± 3.60	274.00 ± 1.00	j
UGC 6728	21	21	IRS	44	7.23	d	45.62	20.65	1.73 ± 0.44	5.68 ± 1.00	j
NGC 2110	160	174	IRS	370	48.87	h	321.50	22.57	75.60 ± 6.70	57.40 ± 4.30	j
NGC 2992	79	147	50	313	7.03	d	93.45	22.00	76.00 ± 5.20	162.00 ± 1.00	j
NGC 3081	51	135	80	266	231.20	i	125.30	23.52	18.00 ± 1.70	171.00 ± 1.20	j
MCG-05-23-016	262	336	IRS	633	105.00	b	335.80	22.47	27.80 ± 0.10	42.90 ± 11.70	j
NGC 3783	140	317	IRS	668	84.81	e	255.20	22.47	31.40 ± 1.30	62.20 ± 0.10	j
NGC 7172	75	245	IRS	265	128.00	b	213.10	22.89	55.00 ± 4.20	73.20 ± 5.90	j

PSF subtraction is ∼15 per cent, which includes also the photometric calibration uncertainty (see Alonso-Herrero et al. 2014, 2016 for further details).

Once we obtained the subarcsecond resolution MIR nuclear fluxes (hereafter nuclear fluxes), we can quantify the circumnuclear MIR emission of the galaxies by subtracting the nuclear emission from the total fluxes. To determine the apertures containing the total flux for each galaxy, we used increasing apertures in order to construct a photometric profile (flux versus aperture radius) and chose the aperture which contains ∼95 per cent of the maximum of the profile. Table 2 shows these total fluxes.

As we have MIR observations obtained with different filters (see Table 2), we used the nuclear fluxes calculated as described above and the *Spitzer*/IRS spectra of the galaxies to obtain homogeneous nuclear fluxes at 8 μm.[8] The process involves using spectral decomposition in AGN, PAH and stellar emission components to estimate the AGN contribution of the IRS spectra. To do so, we used the DEBLENDIRS[9] routine (Hernán-Caballero et al. 2015) and the MIR nuclear fluxes in the various filters as priors to constrain the flux of the AGN component. Once we derived the AGN contribution, we used it to extrapolate our nuclear fluxes to 8 μm for all the galaxies. In Table 3, we list these nuclear fluxes. See Appendix B for further details on the spectral decomposition.

4.2 Comparison with arcsecond resolution MIR data

In order to compare the subarcsecond and arcsecond resolution MIR data, we calculate 8 μm arcsecond resolution nuclear fluxes. To do that, we also used the PSF subtraction method to try to recover the nuclear emission from the lower angular resolution *Spitzer*/IRAC images at 8 μm.[10]

In the case of the IRAC data, we used the core point response functions (PRFs).[11] Note that the core PRFs are the most adequate for the PSF-fitting photometry due to the faithful size and structure of the PRF centre. However, these PRFs do not include the extended region of the PRF wings. Therefore, to take into account the wings, we have used scaled core PRFs to derive the nuclear fluxes and then multiplied them by the factor between the core and the extended PRFs fluxes to obtain realistic values of the nuclear emission. We

[8] We chose 8 μm as our wavelength of reference since this is the wavelength of the *Spitzer* images.
[9] http://www.denebola.org/ahc/deblendIRS/

[10] For the galaxies whose *IRAC* images are saturated, we calculate arcsecond resolution nuclear fluxes from the IRS spectra (see Table 3).
[11] http://irsa.ipac.caltech.edu/data/SPITZER/docs/

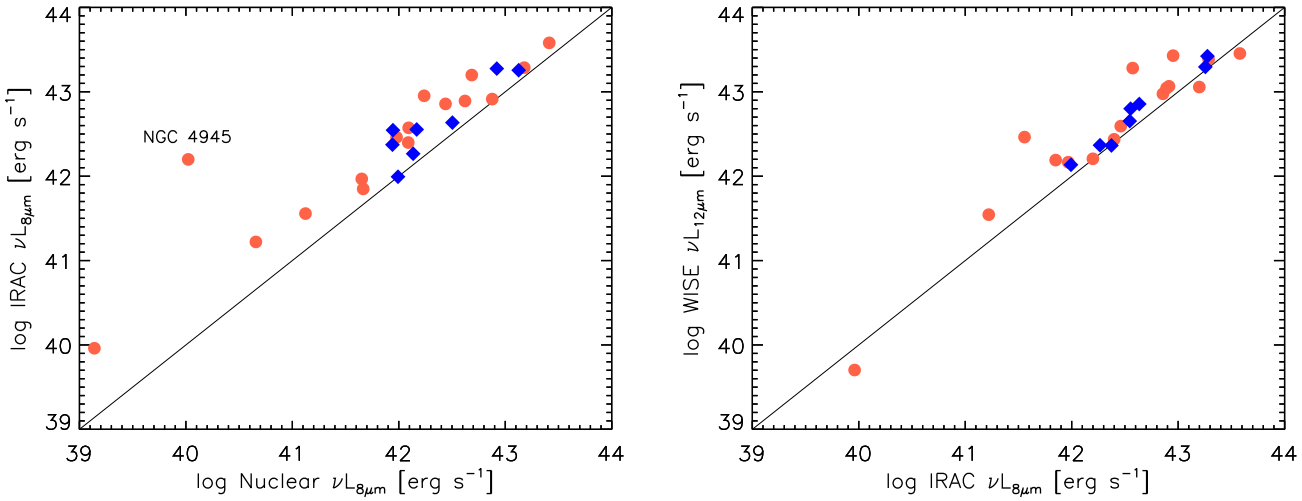

Figure 3. Left-hand panel: arcsecond resolution 8 μm IRAC nuclear luminosities versus subarcsecond resolution nuclear luminosities at 8 μm. Right-hand panel: arcsecond resolution 8 μm IRAC nuclear luminosities versus arcsecond resolution 12 μm *WISE* luminosities. Blue diamonds and red circles are Sy1 and Sy2 galaxies, respectively. We plot the 1:1 line for comparison.

list the arcsecond resolution nuclear fluxes calculated using this method in Table 3 (see Section 4.1 for further details).

In the left-hand panel of Fig. 3, we show the comparison between the arcsecond and subarcsecond resolution nuclear 8 μm luminosities. As expected, the lower angular resolution nuclear fluxes are generally larger than the subarcsecond resolution nuclear fluxes, being the median value of the ratio between subarcsecond and arcsecond resolution nuclear emission 0.44 ± 0.05. Note that the median value of this ratio is smaller for Sy2 (0.38 ± 0.06) than for Sy1 (0.74 ± 0.09) galaxies. We only recover the subarcsecond nuclear fluxes, using the lower angular resolution MIR data, for the galaxies UGC 6728 and NGC 2110. These are the only galaxies in the BCS_{40} sample with a >90 per cent AGN contribution to the *Spitzer*/IRS spectrum (see Appendix B). On the other hand, the point deviating the most from the 1:1 line is NGC 4945, which has the most extended MIR emission of the BCS_{40} sample.

We checked the relation between the arcsecond resolution 8 μm IRAC nuclear emission and the *WISE* photometry (see the right-hand panel of Fig. 3). We retrieved the *WISE* photometry from the *WISE* Source Catalogue,[12] which were performed using a point source profile-fitting (angular resolution ∼6.5 arcsec at 12 μm). We found that the majority of the *WISE* fluxes are larger than the IRAC fluxes, likely due to the larger scales probed by *WISE* and to the possible contribution of the 11.3 μm PAH feature.

We note that we are not taking into account variability effects in the previous comparisons. However, the variability is not expected to be very important in the MIR, according to simulations and observations. Simulations predict longer variability time-scales in the MIR than in the optical (e.g. Hönig & Kishimoto 2011) and, using *Spitzer* data, García-González et al. (2015) found that the contribution of MIR-variable AGN to the general AGN population is small.

[12] http://irsa.ipac.caltech.edu/cgi-bin/Gator/nph-dd

5 MORPHOLOGICAL ANALYSIS

5.1 Parsec-scale morphologies

In Fig. A1 of Appendix A, we show the subarcsecond resolution MIR data for the BCS_{40} sample. We used different methods, which we describe below, to classify the MIR morphologies on scales of ∼400 pc (average value of the sample) using the ground-based MIR images for each galaxy.

First, we classified by eye the extension of the MIR emission following the same method as in Asmus et al. (2014): (a) point-like nucleus with no extended emission; (b) possibly extended emission, marginal extension; and (c) extended emission, with significant and consistent extension. For further details on the high angular resolution morphologies, see Fig. 4 and Fig. A1 of Appendix A. A large fraction of the sample show extended or possibly extended MIR morphologies (83 per cent; see Table 4), with a variety of structures and features. In Appendix A, we also present the comparison

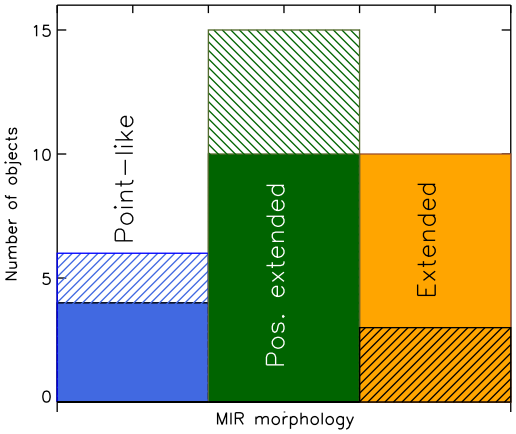

Figure 4. Classification of the BCS_{40} morphologies from the MIR subarcsecond resolution images. The filled and hatched histograms represent the visual and quantitative classifications, respectively. Blue, green and orange histograms correspond to point-like, possibly extended and extended morphologies.

Table 4. MIR morphological classification. Columns 1–4 list the galaxy name, the visual classification, the ratio between nuclear and total fluxes, and the presence or not of PSF subtraction residuals at $\geq 3\sigma$. Column 5 lists the strength of the extended emission, which was calculated by using the ratio between nuclear and total fluxes, and the PSF subtraction residuals. See Section 5.1 for details.

Name	Visual class.	Nuclear versus total flux	Res. Sub 3σ	Quantitative class.
NGC 4395	Pos. ext.	0.76	×	Point-like
NGC 5128	Pos. ext.	0.75	√	Pos. ext.
NGC 4945	Extended	0.04	–	Extended
NGC 4051	Extended	0.93	√	Pos. ext.
NGC 6300	Extended	0.54	√	Pos. ext.
NGC 4388	Pos. ext.	0.69	√	Pos. ext.
NGC 4138	Point-like	0.75	√	Pos. ext.
NGC 4151	Pos. ext.	0.80	√	Pos. ext.
NGC 3227	Extended	0.65	√	Pos. ext.
NGC 7314	Point-like	0.71	×	Point-like
NGC 1365	Extended	0.15	√	Extended
NGC 7582	Extended	0.17	√	Extended
ESO 005-G004	Pos. ext.	0.66	×	Point-like
NGC 7213	Pos. ext.	0.74	×	Point-like
NGC 6814	Point-like	0.73	×	Point-like
MCG-06-30-015	Point-like	0.58	√	Pos. ext.
NGC 5506	Extended	0.78	√	Pos. ext.
UGC 6728	Pos. ext.	0.64	–	Pos. ext.
NGC 2110	Pos. ext.	0.99	√	Pos. ext.
NGC 2992	Extended	0.58	√	Pos. ext.
NGC 3081	Extended	0.67	√	Pos. ext.
MCG-05-23-016	Extended	0.77	√	Pos. ext.
NGC 3783	Pos. ext.	0.78	√	Pos. ext.
NGC 7172	Pos. ext.	0.70	×	Point-like

between the arcsecond and subarcsecond resolution data in the *N* band. In some cases, we can identify similar structures and orientations of the extended MIR emission (ESO 005-G004, NGC 2992, NGC 3227, NGC 3783, NGC 4945 and NGC 7172). However, for the majority of the targets, the IRAC PSF is larger than the extent of the subarcsecond resolution MIR emission. Therefore, the high angular resolution data are crucial to study the circumnuclear emission of Seyfert galaxies.

Secondly, we used the high angular resolution nuclear and total fluxes to evaluate the strength of the nuclear emission against the total emission. To do so, we calculated the compactness factor as the ratio between the nuclear and total flux. Since we have heterogeneous photometry, we calculated the compactness factor for each galaxy using the average ratio of all the bands available. Using this factor and comparing it with the results from the visual classification, we find that our sample is dominated by galaxies whose circumnuclear emission has low surface brightness compared with the nuclear emission (see Fig. 5). The horizontal black dashed line in Fig. 5 corresponds to the minimum value of the compactness factor for point-like morphologies (∼0.6). The overall majority of the extended and possibly extended galaxies are above this value. This is due to the low surface brightness of the extended emission (e.g. MCG-05-23-016, NGC 2992, NGC 3081, NGC 3227, NGC 4051 and NGC 5506). Therefore, in addition to quantitative methods, it is important to perform visual classifications in order to detect low surface brightness extended MIR emission when present. On the other hand, there are few galaxies with bright extended emission (see Table 4 and Fig. 5).

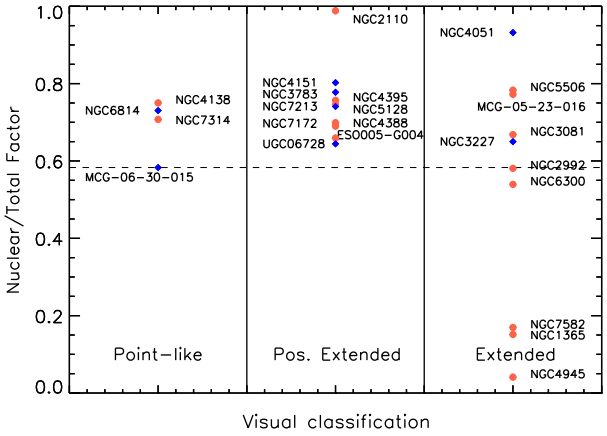

Figure 5. Comparison between the morphological classifications by eye and using the nuclear versus high angular resolution total flux ratio. Blue diamonds and red circles are Sy1 and Sy2 galaxies, respectively. The horizontal black dashed line corresponds to the minimum value of the compactness factor for point-like morphologies.

Thirdly, we use the residuals from the PSF subtraction method described in Section 4.1 and we found that most of the galaxies (∼75 per cent) show residuals at $\geq 3\sigma$, which correspond to the circumnuclear emission (see Table 4).

Finally, using the two quantitative methods described above, we can calculate the strength of the extended emission and compare it with the visual classification. Thus, by using the nuclear to total flux ratio and the 3σ residuals, we consider the MIR morphologies: (1) point-like, when there is ≥50 per cent nuclear contribution to the total flux and no 3σ residuals; (2) possibly extended, when there is ≥50 per cent nuclear contribution to the total flux and 3σ residuals; and (3) extended, when there is ≤50 per cent nuclear contribution to the total flux and 3σ residuals. The result of this classification is shown in Table 4 and Fig. 4.

Using different methods to classify the MIR morphologies, we found, from visual classification, that the majority of the sample show extended or possibly extended morphologies (83 per cent) and 17 per cent are point-like. From the quantitative classification, we found that most of the galaxies present extended or possibly extended emission (75 per cent) and 25 per cent are point-like. Therefore, there is a good agreement between the results obtained using the qualitative and quantitative methods (see Fig. 4). This extended emission represents, on average, ∼30 per cent of the total emission of the BCS_{40} sample (∼25 per cent for Sy1 and ∼30 per cent for Sy2).

We found that 87 per cent of the Sy2 in the BCS_{40} show extended MIR morphologies, versus 75 per cent for Sy1 galaxies. We used the Fisher's exact test method and we found that this difference is not significant.

The percentage of point-like morphologies measured for the BCS_{40} sample is in agreement with the results reported by Asmus et al. (2014) for a sample of 204 AGN detected in the MIR with ground-based instruments (19 per cent). However, we found a larger contribution of extended or possibly extended MIR morphologies (75–83 per cent of the BCS_{40} sample) than the 47 per cent (21 per cent extended and 26 per cent possibly extended) reported by Asmus et al. (2014).[13] The differences between the MIR

[13] The remaining 34 per cent of the sample studied in Asmus et al. (2014) corresponds to galaxies with unknown extension due to insufficient data.

morphologies of the two samples could be related with a distance effect, since the median value of the distance for the sample analysed by Asmus et al. (2014) is 71.7 Mpc, whereas for our sample is 24.1 Mpc.

Previous studies of LIRGs and ULIRGs based on ground-based MIR data as those presented here concluded that AGN are, in general, less extended than SF-dominated systems (e.g. Díaz-Santos et al. 2010; Díaz-Santos et al. 2011; Imanishi et al. 2011). Díaz-Santos et al. (2010) found that, on average, the MIR continuum becomes more compact than the PAH emission as the MIR is increasingly dominated by the AGN. In Imanishi et al. (2011), the authors studied a sample of 18 ULIGRs and found that SF-dominated galaxies have more extended emission, with low surface brightnesses, than AGN-dominated galaxies, which show more compact MIR morphologies. Soifer et al. (2001) found different sizes (ranging from 100 pc to 1.5 kpc) for the MIR emission using ground-based data of a sample of starburst galaxies. These sizes are in good agreement with our results, as we found that the extended MIR emission in AGN-dominated systems is more compact (300 $\pm$ 100 pc) than in SF-dominated systems (650 $\pm$ 700 pc) and composite galaxies (350 $\pm$ 500 pc). The classification of the galaxies as AGN-dominated, SF-dominated and composite comes from the spectral decomposition of the *Spitzer*/IRS spectra (see Appendix B).

We finally checked whether the different MIR morphologies that we find are related to galaxy inclination and/or luminosity. Using the visual classification method, we found that the galaxies with point-like MIR morphologies are face-on or moderately inclined (b/a~0.4–1.0). On the other hand, the galaxies which are extended in the MIR have different values of b/a, from edge-on to face-on (see top panel of Fig. 6). Regarding the AGN luminosity, we found the galaxies with point-like morphologies having intermediate luminosities within the range covered by the galaxies showing extended morphologies (see bottom panel of Fig. 6).

5.2 Kpc-scale morphologies

Despite the fact that a large fraction of the sample (75–83 per cent) show extended morphologies, most of this extended emission is compact and concentrated close to the nuclear region, and it has low surface brightness compared with the nuclear emission. Only six Sy2 galaxies present extended MIR emission at large scales (>400 pc, which is the sample average value) in the high angular resolution MIR data. These galaxies were previously studied in the MIR: (1) NGC 4945 (Imanishi et al. 2011); (2) NGC 1365 (Alonso-Herrero et al. 2012); (3) NGC 7582 (Wold & Galliano 2006; Wold et al. 2006); (4) NGC 5506 (Roche et al. 2007); (5) NGC 2992 (García-Bernete et al. 2015); and (6) NGC 3081 (Ramos Almeida et al. 2011a). Here we make a comparison between this large-scale MIR emission as detected in the arcsecond and subarcsecond resolution data. In Fig. 7, we show the arcsecond resolution 8 μm IRAC or 12μm *WISE* images and the subarcsecond resolution *N*- and *Q*-band images of these galaxies. The extended emission detected in the high angular resolution data has a similar structure and orientation than those detected in the IRAC or *WISE* images on the same scales (see Fig. 7). For four/six of these galaxies (NGC 1365, NGC 2992, NGC 4945 and NGC 7582), the bulk of this extended emission is due to SF activity, while for NGC 3081 and NGC 5506 is mainly produced by the AGN activity. Although these four galaxies show strong PAH features in their IR spectra, there are other galaxies in the sample with strong PAH features as well which do not show extended emission at large scales (e.g. NGC 7172 and ESO 005-G004). Perhaps, the circumnuclear regions of these six galaxies are dustier than the rest. See Appendix C for details on the extended emission of these six objects.

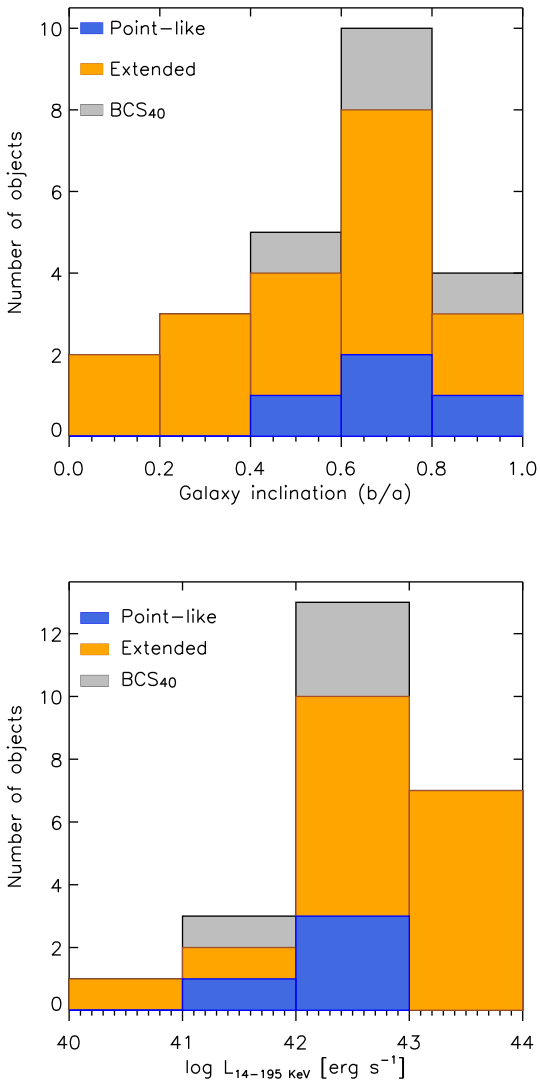

Figure 6. Top panel: galaxy inclination (b/a) distribution of the BCS_{40} sample. Bottom panel: 14-195 keV X-ray luminosity distribution of the sample. The blue and orange filled histograms are the distributions of point-like and extended MIR morphologies, respectively. The grey filled histograms correspond to the total BCS_{40} sample.

We also used the IRAC images to compare the luminosities of the kpc-scale MIR extended emission of Seyfert galaxies with those of normal galaxies. To do so, we calculated IRAC 8 μm total fluxes[14] for the galaxies in our sample that have IRAC data and we found a median value of $\log(\nu L_{8\,\mu m})$=43.17 $\pm$ 0.06 erg s^{-1}. The median value reported by Muñoz-Mateos et al. (2009) for 70 nearby galaxies in the SIRTF Nearby Galaxy survey (SINGs) sample (Kennicutt et al. 2003) is $\log(\nu L_{8\,\mu m})$=42.52 $\pm$ 0.11 erg s^{-1}. As expected, the total MIR luminosity of Seyfert galaxies is higher than in normal galaxies, due to the AGN contribution. If we subtract the IRAC nuclear luminosities from our total luminosities, we measured $\log(\nu L_{8\,\mu m})$=43.06 $\pm$ 0.10 erg s^{-1} for the extended emission, which remains larger than the value reported for the SINGs sample.

[14] To determine the total fluxes, we used the same method as in Section 4.1.

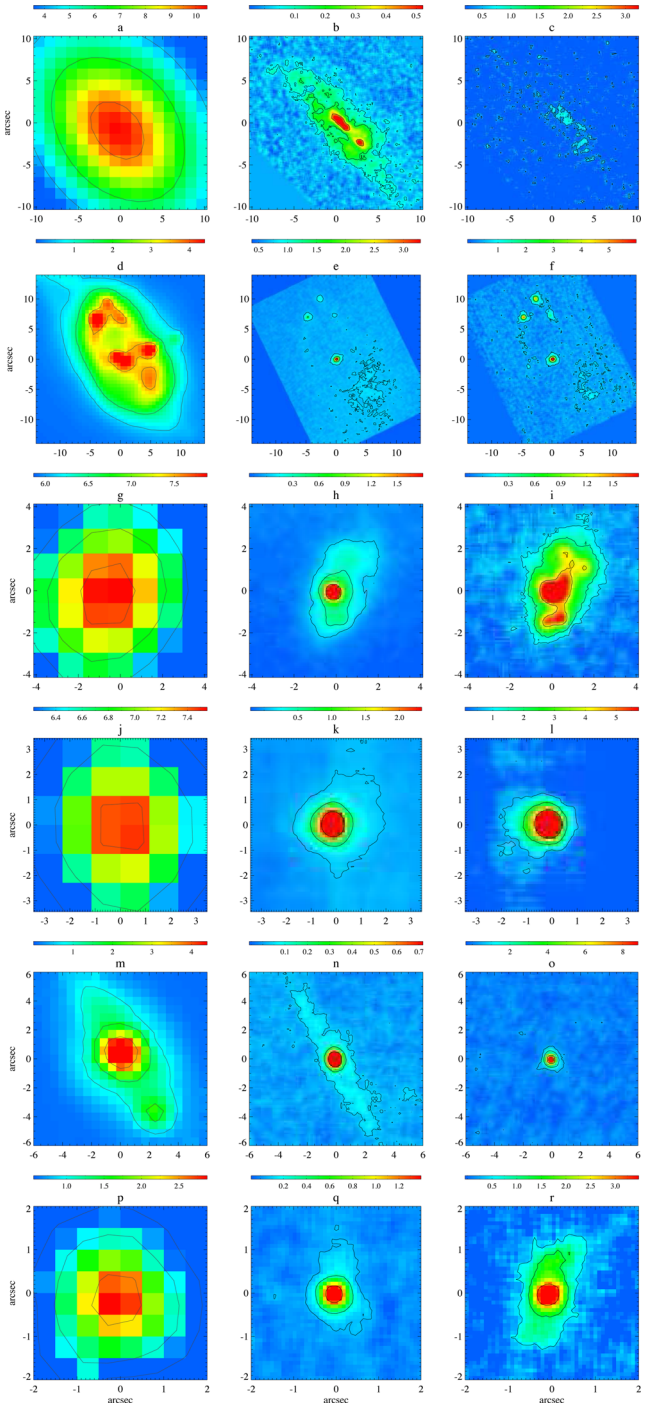

Figure 7. Galaxies showing extended MIR emission on scales larger than 400 pc in the high angular resolution data. From left to right: arcsecond resolution data, *N*- and *Q*-band subarcsecond resolution data. (a)–(c) NGC 4945; (d)–(f) NGC 1365; (g)–(i) NGC 7582; (j)–(l) NGC 5506; (m)–(o) NGC 2992; (p)–(r) NGC 3081. All images have been smoothed (3 pixel box). Colour bars correspond to fluxes in mJy pixel^{-1} units. North is up, and east to the left.

This is likely due to the extra contribution of AGN-heated dust in the circumnuclear region of the galaxies in our sample.

Finally, using the arcsecond resolution data, we also classified the sample morphologies as: (1) irregular; (2) point-like; (3) elliptical; and (4) spiral. We found that ∼60 per cent of the sample present spiral morphologies (see Table 5). In Table 5, we have also indicated whether or not the galaxies show a compact nucleus. Using this classification, we found that all the galaxies without a compact nucleus have extended morphologies according to our visual classification of the subarcsecond resolution data.

Table 5. Arcsecond resolution MIR morphological classification. Columns 1–3 list the galaxy name, the visual classification and if the galaxy show a compact nucleus or not.

Name	Visual morph.	Compact nucleus
NGC 4395	Irregular	√
NGC 5128	Spiral	×
NGC 4945	Spiral	×
NGC 4051	Spiral	√
NGC 6300	Spiral	√
NGC 4388	Spiral	√
NGC 4138	Spiral	√
NGC 4151	Spiral	√
NGC 3227	Spiral	×
NGC 7314	Spiral	√
NGC 1365	Spiral	×
NGC 7582	Elliptical	×
ESO 005-G004	Elliptical	×
NGC 7213	Spiral	√
NGC 6814	Spiral	√
MCG-06-30-015	Point-like	√
NGC 5506	Point-like	√
UGC 6728	Irregular	√
NGC 2110	Irregular	×
NGC 2992	Elliptical	×
NGC 3081	Spiral	√
MCG-05-23-016	Point-like	√
NGC 3783	Spiral	√
NGC 7172	Elliptical	×

6 MIR CORRELATIONS WITH AGN AND SF INDICATORS

Dust grains in the nuclear region of AGN are heated mainly by nuclear activity, although other heating sources can be SF and/or jets. This radiation is re-emitted in the IR range, peaking in the MIR. On the other hand, due to the high energies involved in the accretion process, X-rays are good tracers of the AGN power. For this reason, the X-ray MIR correlation has been widely used in the literature to investigate the origin of the MIR emission in different types of AGN (Lutz et al. 2004; Ramos Almeida et al. 2007; Horst et al. 2008; Gandhi et al. 2009; Levenson et al. 2009; Ichikawa et al. 2012; Mason et al. 2012; Matsuta et al. 2012; Sazonov et al. 2012; Asmus et al. 2015; Mateos et al. 2015).

Another AGN tracer commonly used is [O IV] λ25.89 μm (IP∼55 eV; Spinoglio & Malkan 1992; Spinoglio et al. 2012), which correlates well with both the hard X-rays (Meléndez et al. 2008a; Diamond-Stanic et al. 2009; Rigby et al. 2009) and the soft X-rays (Prieto, Pérez García & Rodríguez Espinosa 2002). The [O IV] emission line has proved to be an accurate indicator of the AGN luminosity (see Weaver et al. 2010 and references therein), and particularly in the case of Seyfert galaxies (Pereira-Santaella et al. 2010).

On the other hand, low IP MIR emission lines such as [Ne II] λ12.81 μm (IP∼21 eV) are used to quantify the SFR of Seyfert galaxies (Spinoglio & Malkan 1992; Ho & Keto 2007; Pereira-Santaella et al. 2010; Spinoglio et al. 2012). However, for

Table 6. Correlation properties of the BCS_{40} sample. Column 1 corresponds to the quantities given the abscissa of Figs 8 and 9 whereas the ordinate is the nuclear $L_{8\,\mu m}$ emission. Columns 2 and 3 list the samples considered and the number of galaxies included, respectively. R, P_{null} and σ correspond to the Pearson's correlation coefficient, the null probability and the standard deviation. a and b are the fitting parameters of $\log(Y) = a \times \log(X)+b$. Note that we used the Bucley–James least-squares linear regression method implemented in the ASURV survival analysis package (Feigelson & Nelson 1985; Isobe, Feigelson & Nelson 1986). * and † correspond to the BCS_{40} sample, but excluding NGC 4395 and the AGN-dominated sources, respectively.

X	Sample	N	R	P_{null}	σ	a	b
$L_{2-10\,KeV}$	BCS_{40}	24	0.83	$<1.0 \times 10^{-6}$	0.51	0.75 ± 0.11	10.89
$L_{2-10\,KeV}$	$BCS_{40}^\star$	23	0.74	6.4×10^{-5}	0.51	0.68 ± 0.14	13.68
$L_{2-10\,KeV}$	Type 1	8	0.83	1.1×10^{-2}	0.48	1.41 ± 0.39	−17.10
$L_{2-10\,KeV}$	Type 2	16	0.86	1.7×10^{-5}	0.50	0.72 ± 0.11	12.24
$L_{14-195\,KeV}$	BCS_{40}	24	0.93	$<1.0 \times 10^{-6}$	0.26	0.62 ± 0.05	16.41
$L_{14-195\,KeV}$	$BCS_{40}^\star$	23	0.88	$<1.0 \times 10^{-6}$	0.26	0.58 ± 0.07	18.21
$L_{14-195\,KeV}$	Type 1	8	0.75	3.4×10^{-2}	0.32	0.71 ± 0.26	12.82
$L_{14-195\,KeV}$	Type 2	16	0.96	$<1.0 \times 10^{-6}$	0.24	0.63 ± 0.05	16.03
$L_{[O\,IV]}$	BCS_{40}	24	0.84	$<1.0 \times 10^{-6}$	0.48	0.74 ± 0.10	9.23
$L_{[O\,IV]}$	$BCS_{40}^\star$	23	0.78	1.2×10^{-5}	0.49	0.74 ± 0.13	9.08
$L_{[O\,IV]}$	Type 1	8	0.81	1.4×10^{-2}	0.36	1.01 ± 0.29	−2.35
$L_{[O\,IV]}$	Type 2	16	0.89	5.0×10^{-6}	0.48	0.77 ± 0.11	8.07
$L_{[Ne\,II]SF}$	$BCS_{40}^\dagger$	16	0.39	1.4×10^{-1}	0.68	0.29 ± 0.19	27.83

luminous AGN, there is a significant contribution of the AGN to the [Ne II] λ12.81 μm emission (Pereira-Santaella et al. 2010). We refer the reader to Roche et al. (1991), Spinoglio & Malkan (1992), Ho & Keto (2007), Pereira-Santaella et al. (2010), Dasyra et al. (2011) and Spinoglio et al. (2012) for further discussion on the MIR diagnostics described above.

It is interesting then to correlate different AGN and SF indicators with the MIR nuclear and circumnuclear emission of Seyfert galaxies to investigate the dominant heating source of the dust. With this aim, we compiled X-ray luminosities (the intrinsic 2–10 and 14–195 keV) and integrated MIR emission line luminosities ([O IV] λ25.89 μm and [Ne II] λ12.81 μm) for our sample (see Table 3) and we performed linear regressions in log–log space (see Table 6). We note that, although hereafter we will refer to luminosity–luminosity correlations only, we confirmed that the results hold in flux–flux space (see Table D1 of Appendix D).

In the left-hand panels of Fig. 8, we show the relation between the high angular resolution MIR nuclear emission and the intrinsic 2–10 and 14–195 keV X-ray emission. As can be seen from the top-left panel of Fig. 8, there is a tight correlation between the MIR nuclear luminosities and the intrinsic 2–10 keV X-ray emission (Pearson's correlation coefficient $R = 0.83$). This correlation improves when we use the harder 14–195 keV X-ray luminosity ($R = 0.93$; bottom-left panel of Fig. 8 and Table 6). The tight correlations shown in the left-hand panels of Fig. 8 suggest that our nuclear MIR fluxes are AGN-dominated. Points deviating from this correlation indicate the presence of other heating sources (i.e. SF and/or jets) on the scales probed by the data (the inner ∼70 pc).

The slope of the nuclear 8 μm–2–10 keV correlation is 0.75 ± 0.11, in agreement with previous studies of Seyfert galaxies using similar MIR wavelengths (6–12 μm; e.g. Lutz et al. 2004; Ramos Almeida et al. 2007; Horst et al. 2008; Gandhi et al. 2009; Levenson et al. 2009; Sazonov et al. 2012). For example, Ramos Almeida et al. (2007) found a slope of 0.8 by using nuclear fluxes obtained from ISOCAM data at 6.75 μm. Using high angular resolution 12 μm fluxes from VISIR, Horst et al. (2008) and Gandhi et al. (2009) found slopes of ∼1 and 0.9, respectively. Finally, Levenson et al. (2009) reported a value between 0.7 and 0.9 for this slope by employing different methods to obtain nuclear fluxes at 8–12 μm using data from the Gemini telescopes.

We also find good nuclear MIR–hard X-ray correlations when we perform the fits for the Sy1 and Sy2. In the case of the MIR–2–10 keV correlation, we measure slopes of 1.4 ± 0.4 and 0.7 ± 0.1 for Sy1 and Sy2 ($R = 0.83$ and 0.86, respectively). This difference practically disappears when we use the 14–195 keV luminosity (see bottom-left panel of Fig. 8). In this case, we measure slopes of 0.7 ± 0.3 and 0.6 ± 0.1 for Sy1 and Sy2, with $R = 0.75$ and 0.96, respectively. The less significant correlation that we found for the Sy1 is likely a consequence of the small number of objects. We conclude that the fits to the Sy1 and Sy2 galaxies are consistent with each other, indicating that the nuclear 8 μm emission of Seyfert galaxies is essentially independent of the viewing angle and line-of-sight obscuration and nearly isotropic on the small scales probed here (the inner ∼70 pc). We have also compared the nuclear MIR luminosity distributions of Sy1 and Sy2 galaxies using the Kolmogorov-Smirnov (KS) test and we do not find significant differences between the two Seyfert types. This is in agreement with the predictions from clumpy torus models and with observational results: the nuclear 8–18 μm SEDs of Sy1 and Sy2 galaxies are almost identical (e.g. Nenkova et al. 2008a,b; Ramos Almeida et al. 2011b).

As we have quantified the circumnuclear emission of the galaxies, we can do the same exercise to investigate the heating source of this MIR extended emission. However, in the case of the circumnuclear emission, we have heterogeneous photometry (i.e. fluxes measured in different filters), and therefore we cannot perform linear fits as we did for the nuclear fluxes.[15] Thus, we separated the circumnuclear luminosities in three bands (8–11, 11–14 and 17–19 μm) and plotted them in the right-hand panels of Fig. 8, with different colours indicating different wavelengths, versus the hard X-ray

[15] We derived nuclear fluxes at 8 μm by combining the high angular resolution data and spectral decomposition of the *Spitzer* spectra, but unfortunately, we cannot do the same for the circumnuclear emission.

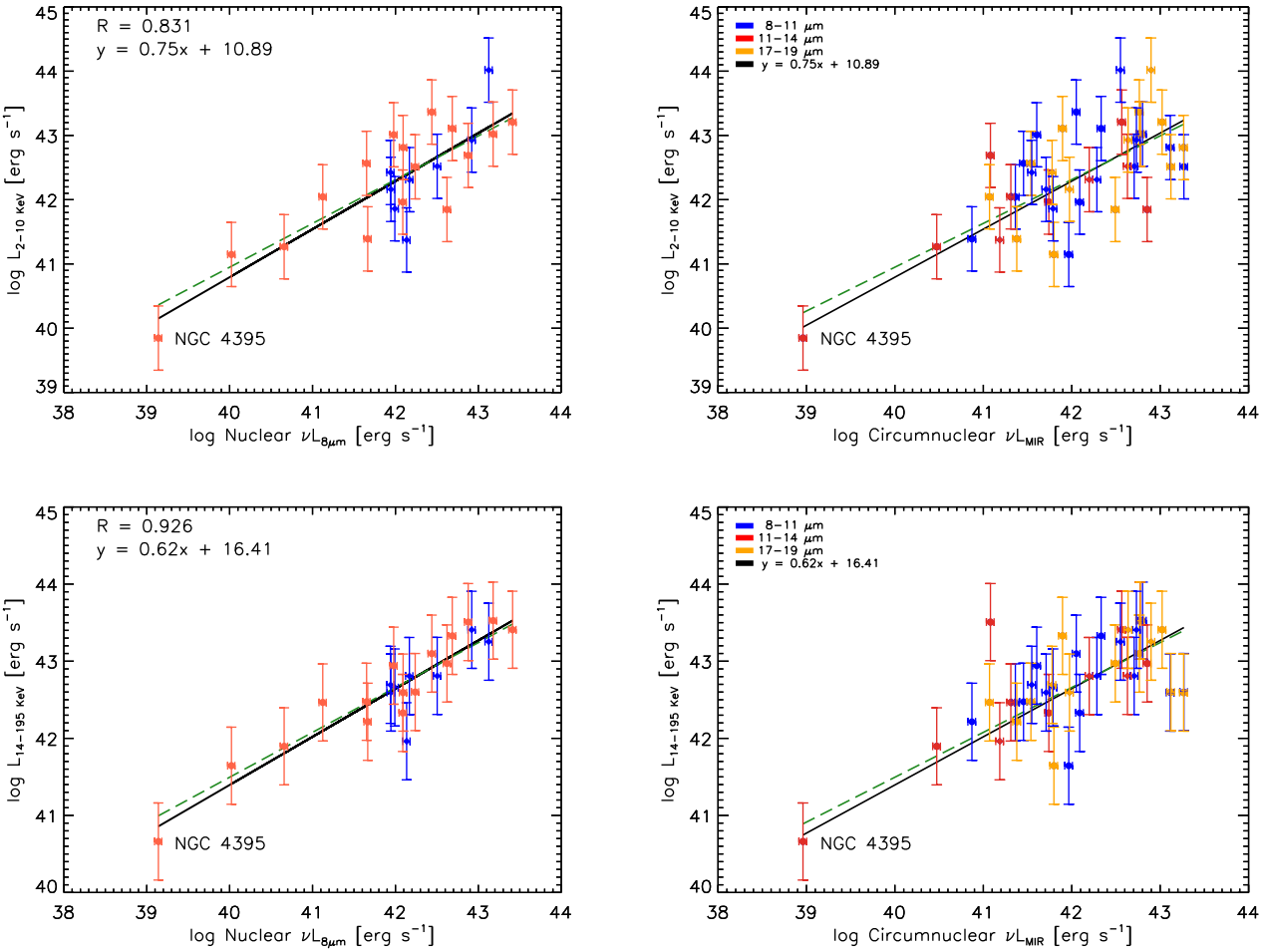

Figure 8. High angular resolution MIR–X-ray luminosity correlations. Top-left panel: 8 μm nuclear luminosity versus intrinsic 2–10 keV X-ray luminosity. Bottom-left panel: same as in the top-left panel, but for the 14–195 keV X-ray luminosity. Right-hand panels: same as in the left-hand panels, but for the circumnuclear MIR luminosities, with different colours indicating different wavelengths. The black lines correspond to the nuclear correlation results from the fits shown in the left-hand panels. The green dashed lines correspond to the same fit, but excluding NGC 4395. Blue diamonds and red circles are Sy1 and Sy2 galaxies, respectively. The vertical error bars correspond to one order of magnitude, which is the uncertainty associated with multi-epoch X-ray measurements. The horizontal error bars correspond to the photometry uncertainty reported in Section 4.1.

luminosities. We show the results from the nuclear fits (those in the left-hand panels of Fig. 8) for comparison, and in order to investigate the scatter of the circumnuclear luminosities, we measured the mean absolute deviations of this emission from the nuclear fits (see Table 6).

In general, there is also a correlation between the circumnuclear MIR and hard X-ray luminosity (at 2–10 and 14–195 keV), although with more scatter than that of the nuclear MIR emission. The mean absolute deviations from the nuclear fits are 0.63 and 0.56 for the 2–10 and 14–195 keV luminosities, respectively. Indeed, some of the points deviating more from the nuclear fits correspond to the galaxies whose extended MIR emission is mainly produced by SF (see Appendices B and C). Therefore, for the majority of the galaxies, we find that the AGN is the main contributor to their circumnuclear emission (the inner ∼400 pc), with some contribution from SF. Other AGN components such as jets and narrow emission line clouds, apart from the dusty torus, emit in the MIR, and this emission can be detected at kpc-scales. For example, in the case of the Sy2 galaxy NGC 1068, Mason et al. (2006) detected low-surface brightness MIR emission from dust in the ionization cones extending to hundreds of parsecs.

Another interesting result from the right-hand panels of Fig. 8 is that the correlation seems to be independent of the MIR wavelength chosen. The distribution of the points in the MIR–X-ray plots is similar for the three ranges considered (8–11, 11–14 and 17–19 μm), which is in agreement with the results reported by Ichikawa et al. (2012) using lower angular resolution *AKARI* data. Moreover, the circumnuclear MIR luminosities of the two Seyfert types are almost identical according to the KS test, as we also found for the nuclear luminosities. This is also compatible with an AGN-dominated circumnuclear emission.

To further investigate the origin of the nuclear and circumnuclear MIR emission of the sample, in Fig. 9, we show the same correlations as in Fig. 8, but now using the MIR emission lines [O IV] λ25.89 μm and [Ne II] λ12.81 μm instead of X-ray luminosities. We find a tight correlation between the nuclear MIR and [O IV] λ25.89 μm luminosities. Indeed, the slope and Pearson's correlation coefficient are practically identical to those measured for the nuclear 8 μm–2–10 keV fit (top-left panel of Fig. 8 and Table 6). We also measure a steeper slope for Sy1 galaxies (1.0 ± 0.3 with $R = 0.81$) than for Sy2 (0.8 ± 0.1 with $R = 0.89$), but the values are consistent within the errors. Again, the tight correlation between our nuclear MIR

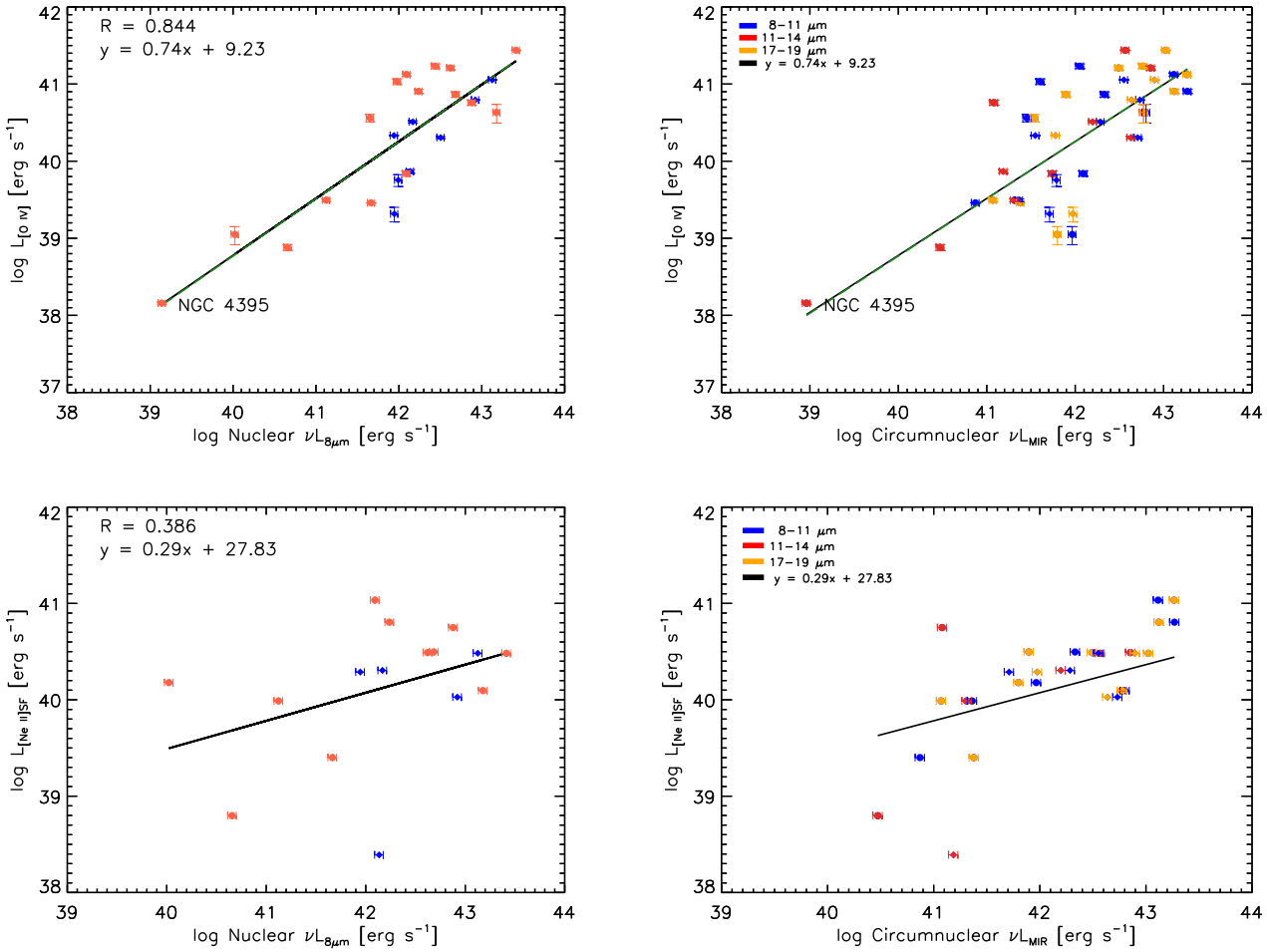

Figure 9. Top-left panel: 8 μm nuclear luminosity versus integrated [O IV] λ25.89 μm emission line luminosity. Bottom-left panel: same but for the integrated [Ne II]$_{SF}$λ12.81 μm emission luminosity. Right-hand panels: same as in the left-hand panels, but for the circumnuclear MIR luminosities. The black lines correspond to the nuclear correlation results from the fits shown in the left-hand panels. The green dashed lines correspond to the same fit, but excluding NGC 4395. Blue diamonds and red circles are Sy1 and Sy2 galaxies, respectively. The vertical error bars correspond to the uncertainties listed in Table 3, and the horizontal error bars correspond to the photometry uncertainty reported in Section 4.1.

luminosities and the [O IV] emission of the galaxies indicates that our nuclear 8 μm fluxes are AGN-dominated.

In order to have a reliable SF activity indicator, we estimated the AGN and SF contributions to the [Ne II] λ12.81 μm emission (hereafter [Ne II]$_{AGN}$ and [Ne II]$_{SF}$, respectively), following the same method as in Meléndez et al. (2008b). We use the [Ne II]–[O IV] correlation[16] for the AGN-dominated systems in our sample (see Appendix B) to estimate [Ne II]$_{AGN}$ fluxes for all the galaxies. We then subtracted these [Ne II]$_{AGN}$ fluxes from the total [Ne II] emission and derived [Ne II]$_{SF}$. From the bottom-left panel of Fig. 9, we see that the correlation between nuclear MIR emission and [Ne II]$_{SF}$λ12.81 μm is less significant ($R = 0.39$) and it has larger scatter than those discussed before. This also indicates that there is little or no contribution of SF to our nuclear MIR fluxes.

Considering the low X-ray and MIR luminosities of the galaxy NGC 4395, which is labelled in Figs 8 and 9, we have checked that the correlations shown in these figures are not due to the presence of this galaxy in the sample (see Table 6). We find almost identical results if we exclude NGC 4395 from the fits (green dashed lines in the previously mentioned figures).

[16] We found the same correlation $\log([\mathrm{Ne\,II}]_{AGN}) = (0.81 \pm 0.16) \times \log([\mathrm{O\,IV}]) + 7.24$ as Meléndez et al. (2008b), within the errors.

Finally, in the right-hand panels of Fig. 9, we show the same correlations, but for the circumnuclear MIR emission, as in the right-hand panels of Fig. 8. We also found a good correlation with the [O IV] λ25.89 μm emission line luminosity, with the mean absolute deviation being identical to those measured for the hard X-rays (0.56). For the [Ne II]$_{SF}$λ12.81 μm line, the distribution of points in the bottom-right panel of Fig. 9 is similar to the nuclear fluxes, with the mean deviation from the nuclear fit being 1.18.

Summarizing, the tightness of the correlations between the nuclear MIR emission and both the X-rays and [O IV], as well as the less significant correlation with [Ne II]$_{SF}$ confirm that the 8 μm emission of the inner ∼70 pc of the BCS$_{40}$ sample is AGN-dominated. We find practically the same correlations, although with larger scatter, for the circumnuclear emission. This suggests that the AGN dominates the MIR emission in the inner ∼400 pc of the galaxies, although with some contribution from SF for the galaxies deviating more from the nuclear correlations.

7 CONCLUSIONS

In this work, we present the first detailed study of the nuclear and circumnuclear MIR emission of a complete sample of Seyfert galaxies (24 galaxies; BCS$_{40}$ sample) selected in the X-rays using

high angular resolution images from 8–10 m-class ground-based telescopes. We also used *Spitzer* and/or *WISE* arcsecond resolution MIR imaging in order to compare the MIR morphologies and nuclear fluxes. Finally, we investigated the relationship of the MIR nuclear and circumnuclear emission with the intrinsic 2–10 keV, the 14–195 keV X-ray emission and different MIR emission lines. The main results are as follows.

(i) Using different methods to classify the MIR nuclear morphologies, we found, from visual classification, that the majority (83 per cent) of the sample show extended or possibly extended morphologies, whereas 17 per cent are point-like. From the quantitative classification, we found that most of the galaxies present extended or possibly extended emission (75 per cent) and 25 per cent are point-like.

(ii) This extended MIR emission is compact and it has low surface brightness compared with the nuclear emission: it represents, on average, ∼30 per cent of the total emission of the BCS_{40} sample (∼25 per cent for Sy1 and ∼30 per cent for Sy2).

(iii) We find that the extended MIR emission in AGN-dominated systems is more compact (300 ± 100 pc) than in SF-dominated systems (650 ± 700 pc) and composite galaxies (350 ± 500 pc).

(iv) Using the visual classification method, we find that the galaxies with point-like MIR morphologies are face-on or moderately inclined (b/a∼0.4–1.0). On the other hand, the galaxies which are extended in the MIR have different values of b/a, from edge-on to face-on.

(v) We find that the MIR emission is practically the same for Sy1 and Sy2, at nuclear and circumnuclear scales. This result is in agreement with the predictions from clumpy torus models if the main heating source of the circumnuclear emission is nuclear activity.

(vi) The tightness of the correlations between the nuclear MIR emission and both the X-rays and [O IV], and the less significant correlation with $[Ne\,II]_{SF}$ confirm that the 8 μm emission of the inner ∼70 pc of the BCS_{40} sample is AGN-dominated.

(vii) We find practically the same correlations, although with slightly larger scatter, for the circumnuclear emission. This suggests that the AGN dominates the MIR emission in the inner ∼400 pc of the galaxies, although with some contribution from SF for the galaxies deviating more from the nuclear correlations.

ACKNOWLEDGEMENTS

IGB acknowledges financial support from the Instituto de Astrofísica de Canarias through Fundación La Caixa. This research was partly supported by a Marie Curie Intra European Fellowship within the 7th European Community Framework Programme (PIEF-GA-2012-327934). CRA and IGB acknowledge financial support from the Spanish Ministry of Science and Innovation (MICINN) through project PN AYA2013-47742-C4-2-P. CRA also acknowledges the Ramón y Cajal Program of the Spanish Ministry of Economy and Competitiveness. AA-H and AHC acknowledges financial support from the Spanish Ministry of Economy and Competitiveness through grant AYA2012-31447 which is partly funded by the FEDER program. AA-H also acknowledges AYA2015-64346-C2-1-P, which is partly funded by the FEDER programme. AHC also acknowledges funding by the Spanish Ministry of Economy and Competitiveness under grants AYA2015-70815-ERC and AYA2012-31277. OGM acknowledges to the PAPIIT project IA100516.

This work is based on observations made with the Gran Telescopio de CANARIAS (GTC), installed in the Spanish Observatorio del Roque de los Muchachos of the Instituto de Astrofísica de Canarias, in the island of La Palma. The GTC/CC programs under which the data were obtained are GTC43-15A and an ESO/GTC large programme (182.B-2005).

The Gemini programs under which the data were obtained are GS-2004A-Q-41, GS-2005A-Q-6,, GN-2006-Q-11, GN-2006-Q-30, GS-2006-Q-62, GS-2007A-DD-7, GN-2007A-Q-49, GS-2009B-Q-43, GN-2010A-C-7, GS-2010B-Q-71, GS-2011B-Q-20 and GS-2012-Q-43. The VLT/VISIR programs under which the data were obtained are 076.B-0599(A), 077.B-0137(A), 078.B-0303(A), 080.B-0860(A), 084.B-0366(E), 086.B-0349(C) and 086.B-0349(D).

This work is also based on observations made with the *Spitzer Space Telescope*, which is operated by the Jet Propulsion Laboratory, Caltech under NASA contract 1407.

The CASSIS is a product of the Infrared Science Center at Cornell University, supported by NASA and JPL.

This publication makes use of data products from the *WISE*, which is a joint project of the University of California, Los Angeles, and the Jet Propulsion Laboratory/California Institute of Technology, funded by the National Aeronautics and Space Administration.

Finally, we are extremely grateful to the GTC staff for their constant and enthusiastic support, and to the anonymous referee for useful comments.

REFERENCES

Adams T. F., 1977, ApJS, 33, 19
Alonso-Herrero A. et al., 2012, MNRAS, 425, 311
Alonso-Herrero A. et al., 2014, MNRAS, 443, 2766
Alonso-Herrero A. et al., 2016, MNRAS, 455, 563
Antonucci R., 1993, ARA&A, 31, 473
Asmus D., Hönig S. F., Gandhi P., Smette A., Duschl W. J., 2014, MNRAS, 439, 1648
Asmus D., Gandhi P., Hönig S. F., Smette A., Duschl W. J., 2015, MNRAS, 454, 766
Binggeli B., Sandage A., Tammann G. A., 1985, AJ, 90, 1681
Brightman M., Nandra K., 2011, MNRAS, 413, 1206
Burtscher L. et al., 2013, A&A, 558, A149
Dasyra K. M., Ho L. C., Netzer H., Combes F., Trakhtenbrot B., Sturm E., Armus L., Elbaz D., 2011, ApJ, 740, 94
de Rosa A. et al., 2012, MNRAS, 420, 2087
Diamond-Stanic A. M., Rieke G. H., 2012, ApJ, 746, 168
Diamond-Stanic A. M., Rieke G. H., Rigby J. R., 2009, ApJ, 698, 623
Díaz-Santos T. et al., 2010, ApJ, 723, 993
Díaz-Santos T. et al., 2011, ApJ, 741, 32
Efstathiou A., Rowan-Robinson M., 1995, MNRAS, 273, 649
Eguchi S., Ueda Y., Awaki H., Aird J., Terashima Y., Mushotzky R., 2011, ApJ, 729, 31
Esquej P. et al., 2014, ApJ, 780, 86
Fazio G. G. et al., 2004, ApJS, 154, 10
Feigelson E. D., Nelson P. I., 1985, ApJ, 293, 192
Gandhi P., Horst H., Smette A., Hönig S., Comastri A., Gilli R., Vignali C., Duschl W., 2009, A&A, 502, 457
García-Bernete I. et al., 2015, MNRAS, 449, 1309
García-González J., Alonso-Herrero A., Pérez-González P. G., Hernán-Caballero A., Sarajedini V. L., Villar V., 2015, MNRAS, 446, 3199
Glasse A. C., Atad-Ettedgui E. I., Harris J. W., 1997, in Ardeberg A. L., ed., Proc. SPIE Conf. Ser. Vol. 2871, Optical Telescopes of Today and Tomorrow. SPIE, Bellingham, p. 1197
González-Martín O. et al., 2013, A&A, 553, A35
Goulding A. D., Alexander D. M., 2009, MNRAS, 398, 1165
Hernán-Caballero A. et al., 2015, ApJ, 803, 109

Ho L. C., Keto E., 2007, ApJ, 658, 314
Hönig S. F., Kishimoto M., 2011, A&A, 534, A121
Hönig S. F., Beckert T., Ohnaka K., Weigelt G., 2006, A&A, 452, 459
Hopkins P. F., Quataert E., 2010, MNRAS, 407, 1529
Horst H., Gandhi P., Smette A., Duschl W. J., 2008, A&A, 479, 389
Houck J. R. et al., 2004, ApJS, 154, 18
Ichikawa K., Ueda Y., Terashima Y., Oyabu S., Gandhi P., Matsuta K., Nakagawa T., 2012, ApJ, 754, 45
Imanishi M., Imase K., Oi N., Ichikawa K., 2011, AJ, 141, 156
Isobe T., Feigelson E. D., Nelson P. I., 1986, ApJ, 306, 490
,Kennicutt R. C., Jr et al., 2003, PASP, 115, 928
Khachikian E. E., Weedman D. W., 1971, Astrofizika, 7, 389
Khachikian E. Y., Weedman D. W., 1974, ApJ, 192, 581
Lagage P. O. et al., 2004, The Messenger, 117, 12
Lebouteiller V., Barry D. J., Spoon H. W. W., Bernard-Salas J., Sloan G. C., Houck J. R., Weedman D. W., 2011, ApJS, 196, 8
Levenson N. A., Radomski J. T., Packham C., Mason R. E., Schaefer J. J., Telesco C. M., 2009, ApJ, 703, 390
Liu T., Wang J.-X., Yang H., Zhu F.-F., Zhou Y.-Y., 2014, ApJ, 783, 106
Lutz D., Maiolino R., Spoon H. W. W., Moorwood A. F. M., 2004, A&A, 418, 465
Martínez-Paredes M. et al., 2015, MNRAS, 454, 3577
Mason R. E., Geballe T. R., Packham C., Levenson N. A., Elitzur M., Fisher R. S., Perlman E., 2006, ApJ, 640, 612
Mason R. E. et al., 2012, AJ, 144, 11
Mateos S. et al., 2015, MNRAS, 449, 1422
Matsuta K. et al., 2012, ApJ, 753, 104
Meléndez M. et al., 2008a, ApJ, 682, 94
Meléndez M., Kraemer S. B., Schmitt H. R., Crenshaw D. M., Deo R. P., Mushotzky R. F., Bruhweiler F. C., 2008b, ApJ, 689, 95
Mould J. R. et al., 2000, ApJ, 529, 786
Mulchaey J. S., Koratkar A., Ward M. J., Wilson A. S., Whittle M., Antonucci R. R. J., Kinney A. L., Hurt T., 1994, ApJ, 436, 586
Muñoz-Mateos J. C. et al., 2009, ApJ, 703, 1569
Nardini E., Risaliti G., 2011, MNRAS, 417, 2571
Nenkova M., Sirocky M. M., Ivezić Ž., Elitzur M., 2008a, ApJ, 685, 147
Nenkova M., Sirocky M. M., Nikutta R., Ivezić Ž., Elitzur M., 2008b, ApJ, 685, 160
Packham C., Radomski J. T., Roche P. F., Aitken D. K., Perlman E., Alonso-Herrero A., Colina L., Telesco C. M., 2005, ApJ, 618, L17
Peeters E., Spoon H. W. W., Tielens A. G. G. M., 2004, ApJ, 613, 986
Pereira-Santaella M., Diamond-Stanic A. M., Alonso-Herrero A., Rieke G. H., 2010, ApJ, 725, 2270
Pier E. A., Krolik J. H., 1992, ApJ, 401, 99
Prieto M. A., Pérez García A. M., Rodríguez Espinosa J. M., 2002, MNRAS, 329, 309
Radomski J. T., Piña R. K., Packham C., Telesco C. M., Tadhunter C. N., 2002, ApJ, 566, 675
Radomski J. T., Piña R. K., Packham C., Telesco C. M., De Buizer J. M., Fisher R. S., Robinson A., 2003, ApJ, 587, 117
Ramos Almeida C., Pérez García A. M., Acosta-Pulido J. A., Rodríguez Espinosa J. M., 2007, AJ, 134, 2006
Ramos Almeida C. et al., 2009, ApJ, 702, 1127
Ramos Almeida C. et al., 2011a, MNRAS, 417, L46
Ramos Almeida C. et al., 2011b, ApJ, 731, 92
Ramos Almeida C. et al., 2014, MNRAS, 445, 1130
Rigby J. R., Diamond-Stanic A. M., Aniano G., 2009, ApJ, 700, 1878
Rivers E., Markowitz A., Rothschild R., 2011, ApJS, 193, 3
Roche P. F., Aitken D. K., Smith C. H., Ward M. J., 1991, MNRAS, 248, 606
Roche P. F., Packham C., Aitken D. K., Mason R. E., 2007, MNRAS, 375, 99
Ruschel-Dutra D., Pastoriza M., Riffel R., Sales D. A., Winge C., 2014, MNRAS, 438, 3434
Sales D. A., Pastoriza M. G., Riffel R., Winge C., 2013, MNRAS, 429, 2634
Sazonov S. et al., 2012, ApJ, 757, 181
Schartmann M., Meisenheimer K., Camenzind M., Wolf S., Henning T., 2005, A&A, 437, 861
Shu X. W., Yaqoob T., Wang J. X., 2010, ApJS, 187, 581
Siebenmorgen R., Heymann F., Efstathiou A., 2015, A&A, 583, A120
Soifer B. T. et al., 2000, AJ, 119, 509
Soifer B. T. et al., 2001, AJ, 122, 1213
Spinoglio L., Malkan M. A., 1992, ApJ, 399, 504
Spinoglio L., Dasyra K. M., Franceschini A., Gruppioni C., Valiante E., Isaak K., 2012, ApJ, 745, 171
Stalevski M., Fritz J., Baes M., Nakos T., Popović L. Č., 2012, MNRAS, 420, 2756
Telesco C. M., Pina R. K., Hanna K. T., Julian J. A., Hon D. B., Kisko T. M., 1998, SPIE, 3354, 534
Telesco C. M. et al., 2003, in Iye M., Moorwood A. F. M., eds, Proc. SPIE Conf. Ser. Vol. 4841, Instrument Design and Performance for Optical/Infrared Ground-based Telescopes. SPIE, Bellingham, p. 913
Tody D., 1986, in Crawford D. L., ed., Proc. SPIE Conf. Ser. Vol. 627, Instrumentation in Astronomy VI. SPIE, Bellingham, p. 733
Tristram K. R. W. et al., 2009, A&A, 502, 67
Tueller J., Mushotzky R. F., Barthelmy S., Cannizzo J. K., Gehrels N., Markwardt C. B., Skinner G. K., Winter L. M., 2008, ApJ, 681, 113
Ueda Y. et al., 2015, ApJ, 815, 1
Vaughan S., Uttley P., Pounds K. A., Nandra K., Strohmayer T. E., 2011, MNRAS, 413, 2489
Weaver K. A. et al., 2010, ApJ, 716, 1151
Winter L. M., Mushotzky R. F., Reynolds C. S., Tueller J., 2009, ApJ, 690, 1322
Winter L. M., Lewis K. T., Koss M., Veilleux S., Keeney B., Mushotzky R. F., 2010, ApJ, 710, 503
Wold M., Galliano E., 2006, MNRAS, 369, L47
Wold M., Lacy M., Käufl H. U., Siebenmorgen R., 2006, A&A, 460, 449
Wright E. L. et al., 2010, AJ, 140, 1868
Wu H., Cao C., Hao C.-N., Liu F.-S., Wang J.-L., Xia X.-Y., Deng Z.-G., Young C. K.-S., 2005, ApJ, 632, L79

APPENDIX A: PC- AND KPC-SCALE MORPHOLOGIES

Here we present the comparison between the arcsecond and the subarcsecond resolution MIR images of the BCS_{40} sample. We have used the ground-based *N*-band images, which are closer in wavelength to the *IRAC* and *WISE* data. A large fraction of the galaxies in the BCS_{40} sample have 8 μm *IRAC* data, but we have used 12 μm *WISE* images when the central part of the *IRAC* image is saturated or when there is no 8 μm *IRAC* data available. In the left-hand panels of Fig. A1, we show the *N*-band high angular resolution images of the sample (central 3.6 arcsec region). In the central panels, we show the same region as in the left-hand panels, but for the arcsecond resolution data, and in the right-hand panels, the central 6 arcsec region for comparison. In some cases, we can identify similar structures and orientations in the subarcsecond and arcsecond resolution MIR data, as e.g. in ESO 005-G004, NGC 2992, NGC 3227, NGC 3783, NGC 4945 and NGC 7172.

We also show the arcsecond resolution MIR images of the BCS_{40} sample in Fig. A2, which we used in the classification reported in Section 5.2.

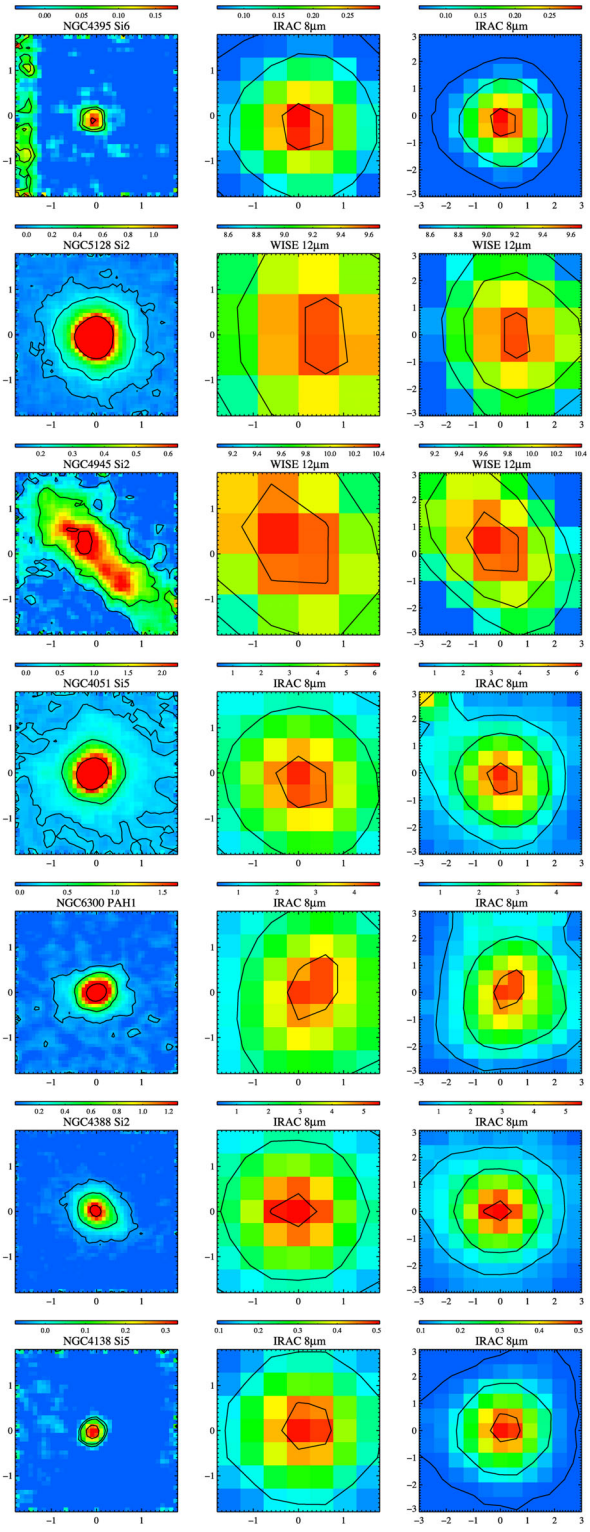

Figure A1. Comparison between the arcsecond and subarcsecond resolution MIR images of the BCS_{40} sample. Left-hand panels: *N*-band high angular resolution images (central 3.6 arcsec region). Central panels: 8 μm *IRAC* or 12 μm *WISE* arcsecond resolution data (central 3.6 arcsec region). Right-hand panels: same as in the central panels, but on a larger scale (central 6 arcsec region). All images are smoothed (box of 3 pixels) and have their own contours overlaid (in black). All images have been smoothed (3 pixel box). Colour bars correspond to fluxes in mJy pixel^{-1} units. North is up, and east to the left.

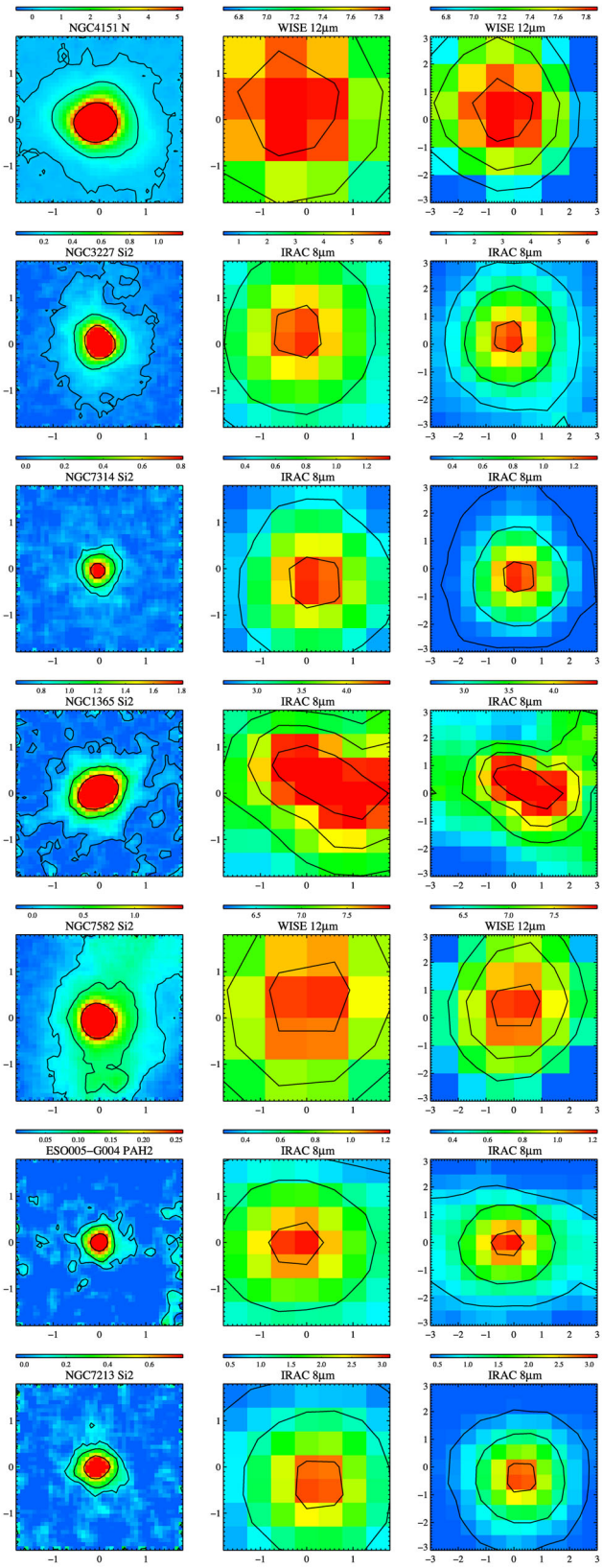

Figure A1 – *continued*

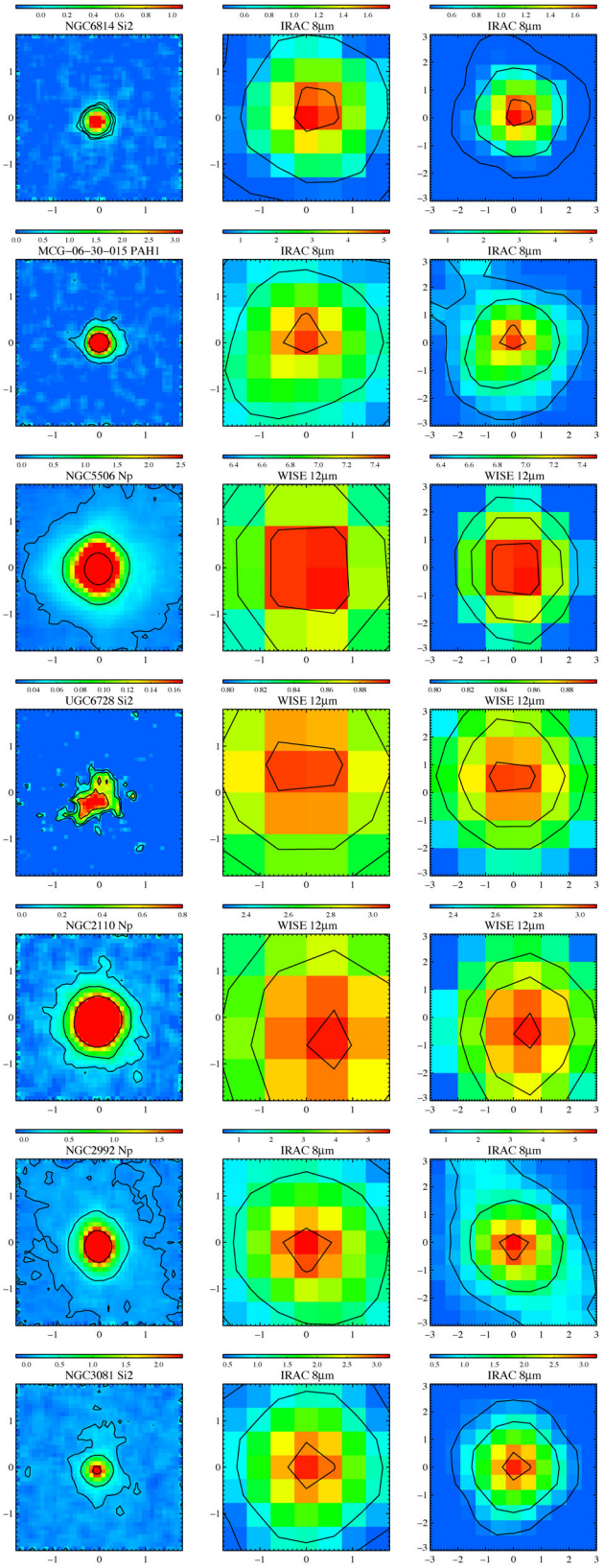

Figure A1 – *continued*

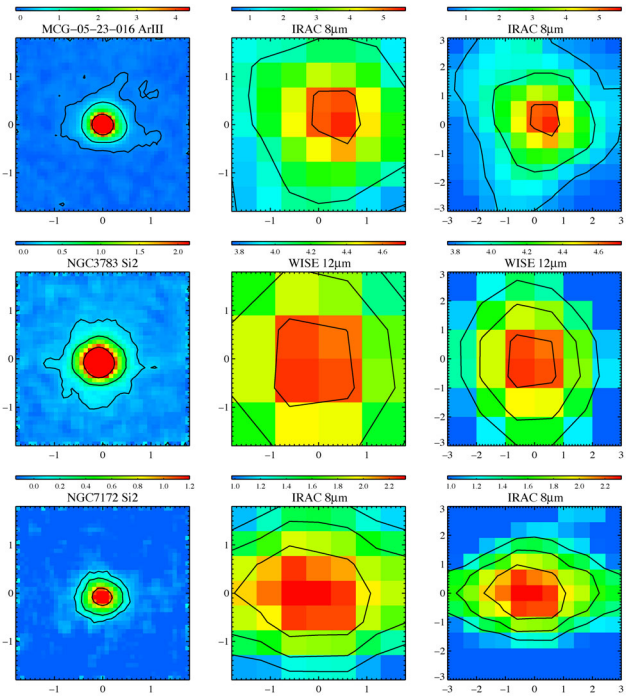

Figure A1 – *continued*

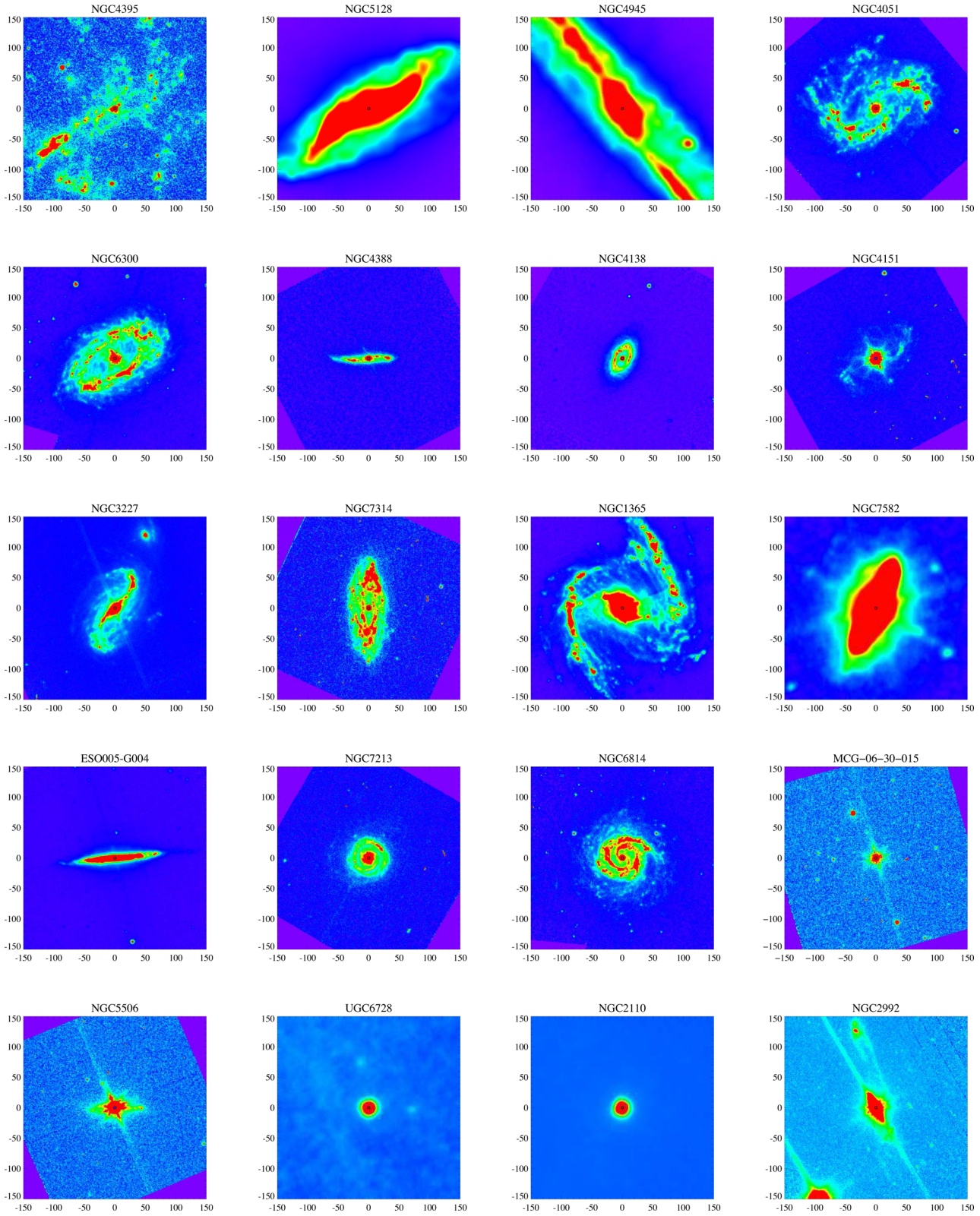

Figure A2. 8 μm *IRAC* or 12 μm *WISE* images of the BCS_{40} sample. The images of NGC 5128, NGC 4945, NGC 7582, UGC 6728 and NGC 2110 correspond to 12 μm *WISE* data. The black square boxes correspond to a size of 3.6 arcsec (the FOV shown in left-hand and central panels of Fig. A1). North is up and east to the left.

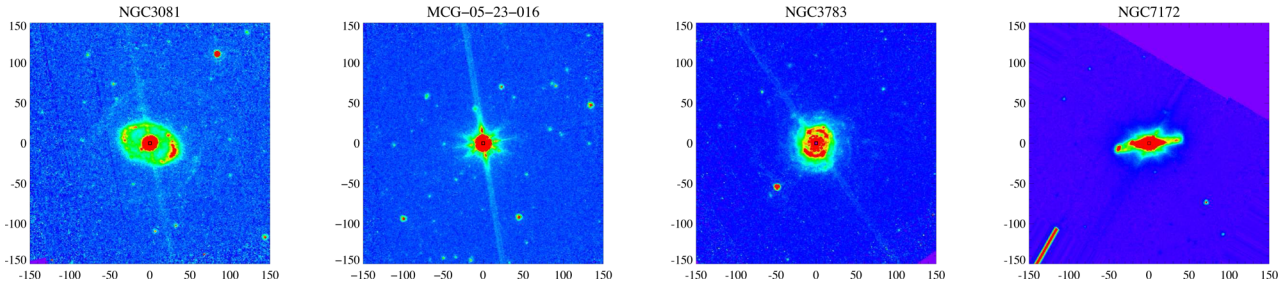

Figure A2 – *continued*

APPENDIX B: SPECTRAL DECOMPOSITION

Here we show the *Spitzer*/IRS spectra of the BCS_{40} sample, which were retrieved from the CASSIS atlas (Lebouteiller et al. 2011). For NGC 4138, there is no low-resolution staring mode spectrum, and instead, we have extracted an spectrum in a 7.7 arcsec aperture diameter from the mapping mode data cube available in the SHA.

Considering the spatial scales probed by the *Spitzer*/IRS spectra of the whole sample ($\leq$650 pc), we expect contribution from both AGN and SF. To estimate the AGN contribution to the *Spitzer*/IRS spectra, we use the DEBLENDIRS routine (Hernán-Caballero et al. 2015), that decomposes MIR spectra using a linear combination of three spectral components: AGN, PAH and stellar emission. We used the high angular resolution MIR nuclear fluxes in the various filters reported in Table 2 as priors to better constrain the AGN component. A detailed description of the method is given in Hernán-Caballero et al. (2015).

We present the results of the *Spitzer*/IRS spectral decomposition of the BCS_{40} sample in Fig. B1. We used the AGN contribution to obtain homogeneous nuclear fluxes at 8 μm using a 1 μm window. These fluxes are presented in Section 4.1. In Table B1, we present the main properties derived from this spectral decomposition.

We found that the majority of the Sy1 have a higher contribution of the AGN than the Sy2 galaxies. The median values of the fractional contribution of the AGN to the *Spitzer*/IRS spectra for Sy1 and Sy2 are 0.82 and 0.62, respectively.

Using the AGN and PAH contributions to the MIR spectra (see Table B1), we can classify the systems as AGN-dominated, when there is $\geq$70 per cent AGN contribution to the MIR spectrum and it does not show PAH emission; and SF-dominated, when there is $\leq$50 per cent AGN contribution to the MIR spectrum and it shows PAH emission. The rest of the galaxies are composite objects. See Table B1 for further details on the systems classification.

In the case of NGC 7213, we cannot obtain a good fit, as the modelling does not reproduce the 9.7 μm silicate emission feature. However, the nuclear MIR fluxes of NGC 7213 are in agreement with the spectral shape of the AGN component derived from the fit.

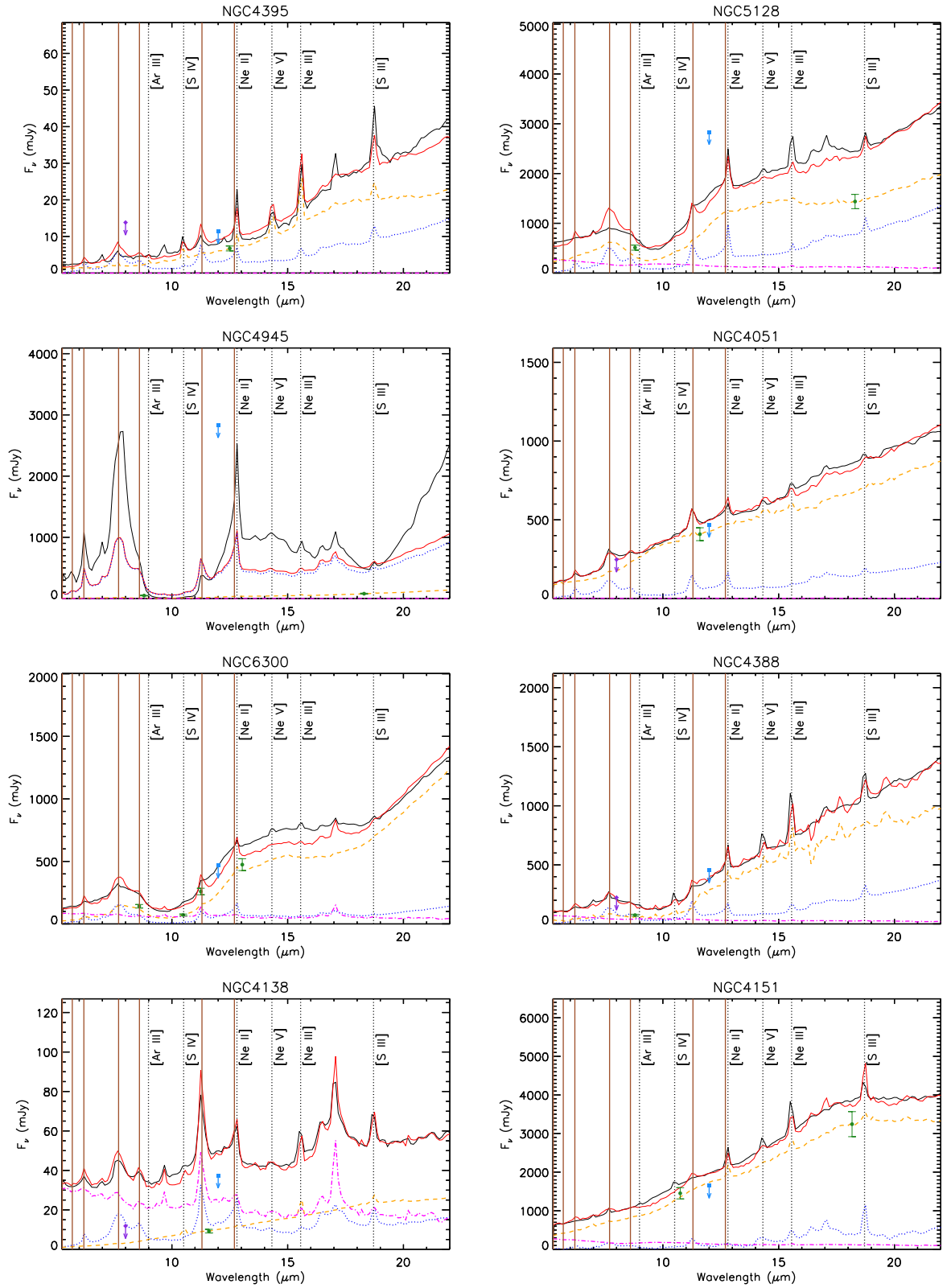

Figure B1. Spectral decomposition of the *Spitzer*/IRS spectra of BCS_{40} sample. We show the *Spitzer*/IRS rest-frame spectra (black solid lines), best fits (red solid lines), AGN component (dashed orange lines), PAH component (dotted blue lines) and stellar component (dot–dashed magenta lines). Green circles are the high angular resolution nuclear fluxes used as priors in the fits. Purple diamonds are the arcsecond resolution 8 μm *IRAC* nuclear fluxes (as upper limit) and blue squares are the arcsecond resolution 12 μm *WISE* fluxes. The brown vertical solid lines correspond to the most important PAH features and the black vertical dotted lines are the main MIR emission lines.

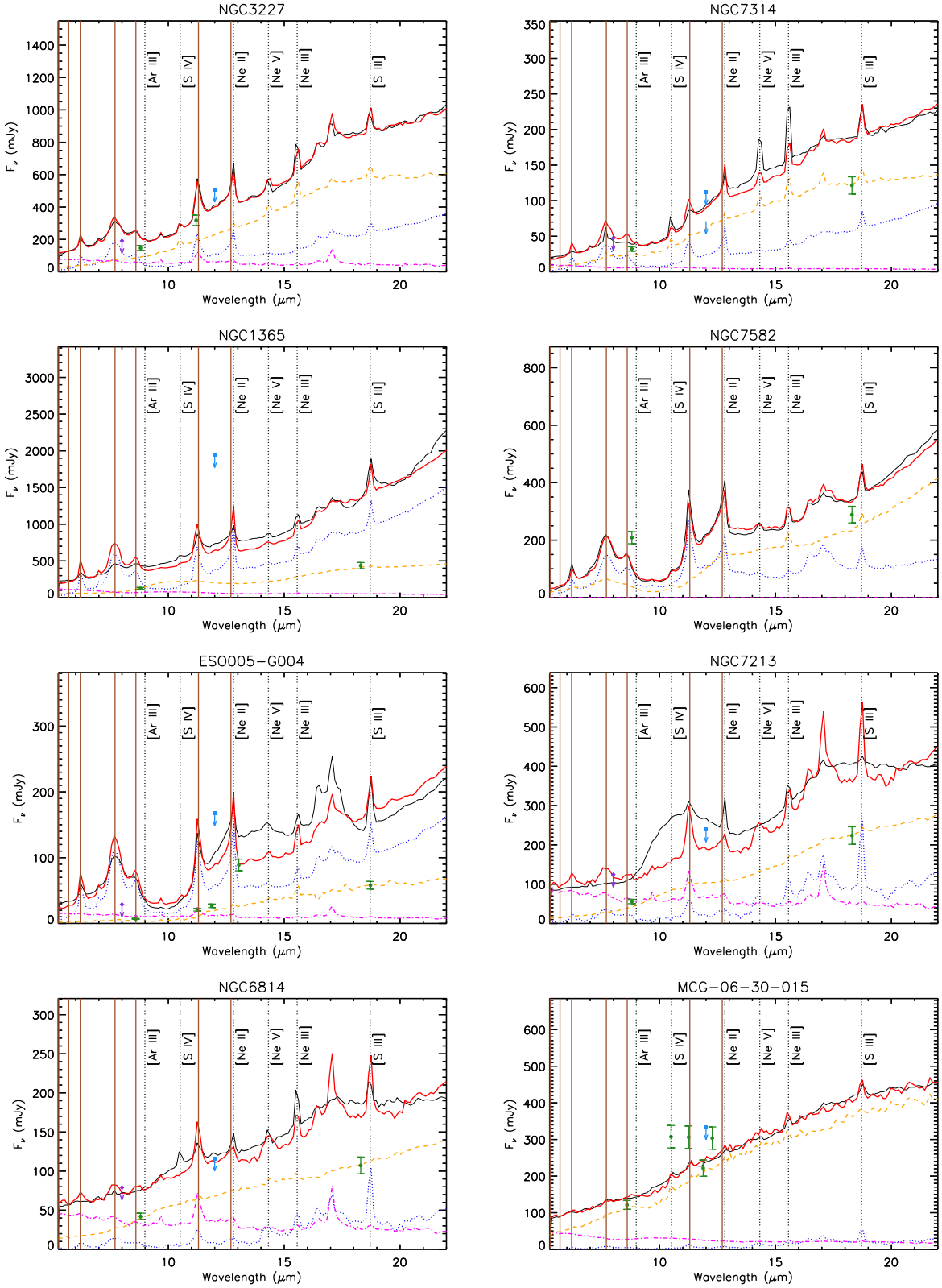

Figure B1 – *continued*

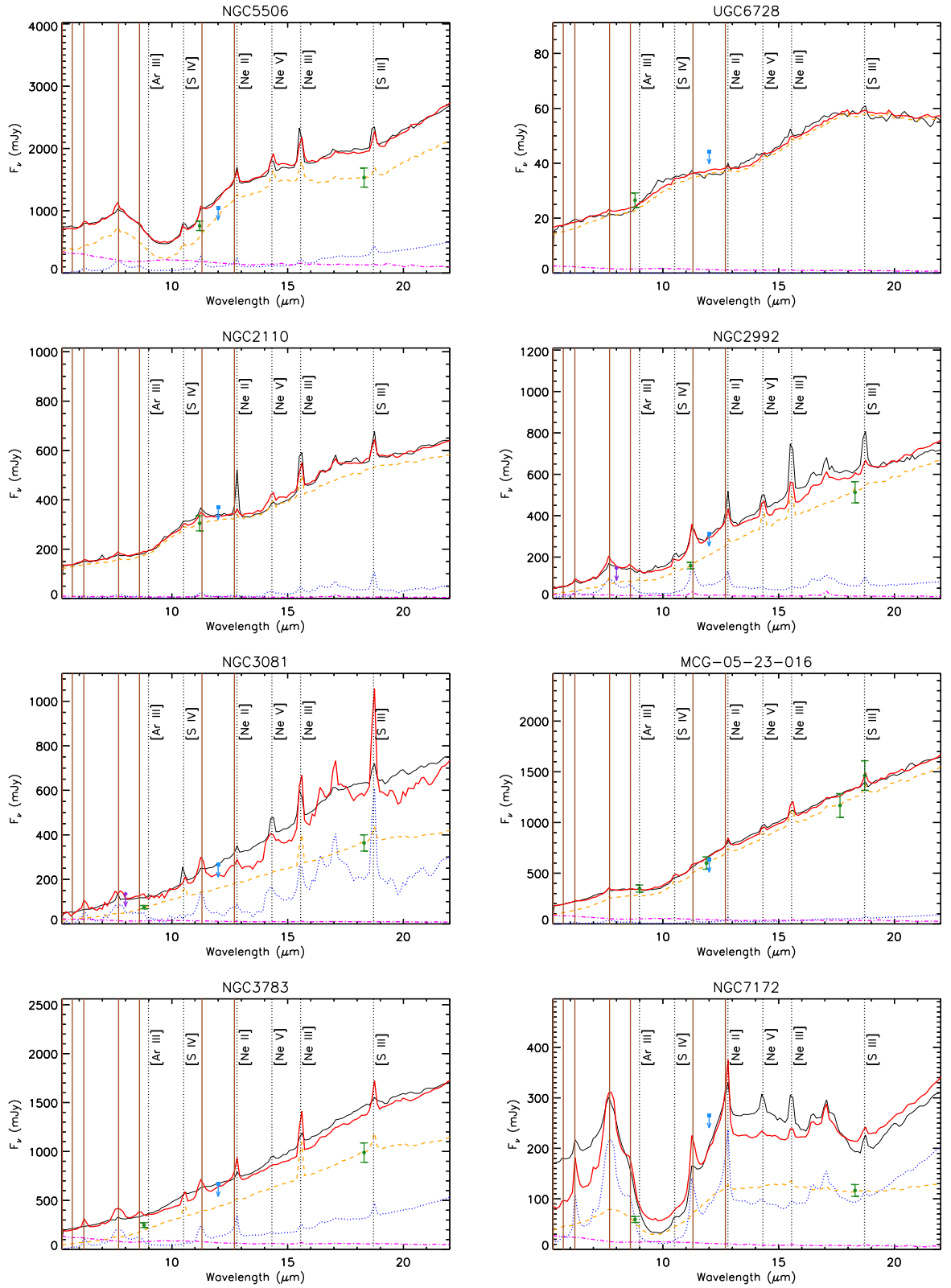

Figure B1 – *continued*

Table B1. Properties derived from the spectral decomposition of the *Spitzer*/IRS spectra of BCS_{40} sample. Columns 2–4 correspond to the fractional contribution of the AGN component, the PAH component and the stellar component to the MIR spectrum, respectively. Columns 5 and 6 list the spectral index of the AGN component and the silicate strength, respectively (positive and negative values correspond to emission and absorption features, respectively). Columns 7 and 8 correspond to the fractional contribution of the AGN component to the rest-frame spectrum at 6 μm and 12 μm, respectively. Column 9 is the same as column 8, but for the PAH component. Finally, column 10 lists the systems classification (see Appendix B for details).

Name	F_{AGN}	F_{PAH}	$F_{Stellar}$	α_{AGN}	S_{Si}	$L_{6\,\mu m}^{AGN}$	$L_{12\,\mu m}^{AGN}$	$L_{12\,\mu m}^{PAH}$	Classification
NGC 4395	0.64	0.36	0.00	−2.83	−0.09	0.62	0.66	0.34	composite
NGC 5128 (CenA)	0.62	0.23	0.15	−1.71	−1.06	0.47	0.67	0.23	composite
NGC 4945	0.05	0.95	0.00	−2.48	−1.36	0.04	0.05	0.95	SF-dominated
NGC 4051	0.85	0.15	0.00	−2.09	0.24	0.83	0.86	0.14	AGN-dominated
NGC 6300	0.62	0.17	0.21	−2.31	−1.50	0.26	0.66	0.17	composite
NGC 4388	0.63	0.23	0.14	−3.71	−1.04	0.27	0.71	0.20	composite
NGC 4138	0.17	0.24	0.59	−2.79	0.20	0.05	0.21	0.28	SF-dominated
NGC 4151	0.83	0.06	0.11	−2.04	−0.08	0.61	0.88	0.05	AGN-dominated
NGC 3227	0.53	0.28	0.19	−2.68	−0.09	0.26	0.57	0.27	composite
NGC 7314	0.62	0.29	0.09	−2.62	−0.33	0.37	0.67	0.27	composite
NGC 1365	0.29	0.57	0.14	−1.92	0.60	0.21	0.32	0.59	SF-dominated
NGC 7582	0.48	0.52	0.00	−2.18	−1.36	0.52	0.48	0.52	SF-dominated
ESO 005-G004	0.18	0.66	0.16	−3.71	−1.04	0.07	0.22	0.65	SF-dominated
NGC 7213	0.45	0.14	0.41	−2.74	0.32	0.15	0.54	0.11	composite
NGC 6814	0.53	0.10	0.37	−2.09	0.24	0.26	0.61	0.07	composite
MCG-06-30-015	0.82	0.03	0.15	−1.91	−0.19	0.54	0.88	0.02	AGN-dominated
NGC 5506	0.72	0.09	0.19	−1.37	−1.19	0.53	0.77	0.09	AGN-dominated
UGC 6728	0.95	0.00	0.05	−1.24	0.12	0.87	0.96	0.00	AGN-dominated
NGC 2110	0.94	0.03	0.03	−1.62	0.18	0.92	0.95	0.02	AGN-dominated
NGC 2992	0.71	0.22	0.07	−2.58	−0.27	0.49	0.71	0.23	composite
NGC 3081	0.63	0.29	0.08	−2.79	0.20	0.38	0.73	0.22	composite
MCG-05-23-016	0.87	0.03	0.10	−2.14	−0.26	0.60	0.90	0.03	AGN-dominated
NGC 3783	0.63	0.21	0.16	−2.79	0.20	0.31	0.68	0.21	composite
NGC 7172	0.45	0.46	0.09	−1.01	−1.06	0.45	0.50	0.45	SF-dominated

APPENDIX C: NOTES ON INDIVIDUAL OBJECTS

Below, we comment on the possible origin of the heating source of the extended emission for the six objects with extended MIR morphologies at large scales (>400 pc, which is the sample average value) in the high angular resolution data presented in Section 5.2. To do so, we first use the arcsecond and subarcsecond resolution images to compare the extended MIR emission structures of these galaxies (see Fig. 7 of Section 5.2). Then, we investigate the origin of the MIR emission using the *Spitzer*/IRS spectra to look for AGN and/or SF activity indicators.

We find that for four of these six galaxies, the bulk of the extended MIR emission is mainly related to SF. On the other hand, for NGC 3081 and NGC 5506, the *Spitzer*/IRS spectra show faint PAH features, weak [Ne II] emission line and prominent AGN tracers. We also found that the majority of these galaxies have a relatively small contribution of AGN emission (<50 per cent) to the *Spitzer*/IRS spectra, except for NGC 2992, NGC 3081 and NGC 5506, which have AGN contributions of 71 per cent, 63 per cent and 72 per cent, respectively (see Appendix B).

NGC 4945 is a practically edge-on spiral galaxy with a highly obscured nucleus containing both an AGN and a starburst. This galaxy presents a bright cluster close to the central region (∼50 pc) and extended emission along PA∼45° out to ∼500 pc in the *N*-band image, being weaker in the *Q* band. NGC 4945 shows the most prominent 6.2 μm PAH feature of the sample and it also presents the 11.3 μm PAH feature and strong [Ne II] emission. On the other hand, there is no significant [S IV] and [Ne V] emission. Therefore, the bulk of the extended MIR emission of this galaxy is mainly SF activity. See Imanishi et al. (2011) for a detailed study of this galaxy.

NGC 1365 is a barred spiral galaxy which presents bright clusters around the nucleus in the *N* and *Q* band, which are also visible in the IRAC image. There is also faint extended emission towards the south (PA∼210°; ∼600 pc from the nucleus) of the *N*- and *Q*-band images, which becomes weaker in the *Q* band and matches that of the IRAC image. The *Spitzer*/IRS spectrum shows strong 6.2 and 11.3 μm PAH features as well as [Ne II] and [Ne III]. This galaxy also presents weak AGN tracers such as [S IV] or [Ne V]. Therefore, we conclude that the bulk of this MIR emission is due to SF activity. See Alonso-Herrero et al. (2012) for a detailed study of this galaxy.

NGC 7582 is a highly inclined barred spiral galaxy. This galaxy has an obscured AGN surrounded by a star-forming disc and a dust lane crossing over the nucleus. The subarcsecond resolution *Q*-band image reveals a bright cluster towards the south, at ∼200 pc from the nucleus, which is not present in the *N*-band image. There is also faint emission extending out to ∼630 pc from the south-east to the north-west (PA∼155°). The *Spitzer*/IRS spectrum shows important 6.2 and 11.3 μm PAH features and also strong [Ne II] emission. On the contrary, the spectrum shows really weak AGN indicators, such as [S IV] and [Ne V]. Therefore, the bulk of this MIR emission is likely related with SF activity. See Wold et al. (2006) and Wold & Galliano (2006) for a detailed study of this galaxy.

NGC 5506 is a practically edge-on spiral galaxy which shows extended MIR emission around the nucleus in the *N*- and *Q*-band images. The high angular resolution *N*-band image reveals faint extended emission from north to south extending out to ∼560 pc. However, there is also faint extended emission towards the east in the *Q*-band image. The *Spitzer*/IRS spectrum of this galaxy shows

Table D1. Same as in Table 6, but in flux–flux space.

X	Sample	N	R	$P_{\rm null}$	σ	a	b
$F_{2-10\,\rm KeV}$	$\rm BCS_{40}$	24	0.64	8.7×10^{-4}	0.49	0.59 ± 0.15	-4.06
$F_{2-10\,\rm KeV}$	$\rm BCS_{40}^{\star}$	23	0.57	4.7×10^{-3}	0.50	0.56 ± 0.18	-4.40
$F_{2-10\,\rm KeV}$	Type 1	8	0.79	1.9×10^{-2}	0.51	1.19 ± 0.38	2.09
$F_{2-10\,\rm KeV}$	Type 2	16	0.63	8.8×10^{-3}	0.46	0.48 ± 0.16	-5.15
$F_{14-195\,\rm KeV}$	$\rm BCS_{40}$	24	0.77	1.3×10^{-5}	0.25	0.44 ± 0.08	-5.36
$F_{14-195\,\rm KeV}$	$\rm BCS_{40}^{\star}$	23	0.74	6.2×10^{-5}	0.26	0.45 ± 0.09	-5.24
$F_{14-195\,\rm KeV}$	Type 1	8	0.79	2.1×10^{-2}	0.23	0.52 ± 0.17	-4.62
$F_{14-195\,\rm KeV}$	Type 2	16	0.80	1.8×10^{-4}	0.25	0.44 ± 0.09	-5.21
$F_{[\rm O\,IV]}$	$\rm BCS_{40}$	24	0.67	3.8×10^{-4}	0.48	0.63 ± 0.15	-5.72
$F_{[\rm O\,IV]}$	$\rm BCS_{40}^{\star}$	23	0.65	8.4×10^{-4}	0.49	0.67 ± 0.17	-5.28
$F_{[\rm O\,IV]}$	Type 1	8	0.84	8.8×10^{-3}	0.36	1.02 ± 0.27	-1.93
$F_{[\rm O\,IV]}$	Type 2	16	0.70	2.2×10^{-3}	0.46	0.61 ± 0.16	-5.81
$F_{[\rm Ne\,II]SF}$	$\rm BCS_{40}^{\dagger}$	16	0.12	6.7×10^{-1}	0.73	0.12 ± 0.27	-11.30

strong [Ne III] and [Ne V] features and faint PAH features. Therefore, we conclude that the origin of this extended MIR emission is likely nuclear activity. See Roche et al. (2007) for a detailed study of this galaxy.

NGC 2992 is an spiral galaxy which is part of the interacting system Arp 245. The high angular resolution *N*-band image reveals faint extended emission along PA$\sim$30° and out to $\sim$2 kpc, which is not present in the *Q* band. This extended emission is also present in the 8 μm *IRAC* image. Considering the strong 6.2 and 11.3 μm PAH features seen in the *Spitzer*/IRS spectrum, the bulk of this extended emission is likely produced by dust heated by SF activity. See García-Bernete et al. (2015) for a detailed study of this galaxy.

NGC 3081 is a barred spiral galaxy which presents extended emission in the *N*- and *Q*-band images, being brighter in the *Q* band. The emission is stronger towards the north, extending out to $\sim$450 pc from the south-east to the north-west (PA$\sim$160°). The *Spitzer*/IRS spectrum of this galaxy shows faint 6.2 and 11.3 μm PAH emission, weak [Ne II] line emission and strong [Ne III], [S IV] and [Ne V] features. Therefore, based on the lack of PAH features in the *Spitzer*/IRS spectrum, we can conclude that the MIR emission of NGC 3081 is mainly produced by nuclear activity. See Ramos Almeida et al. (2011a) for a detailed study of this galaxy.

APPENDIX D: FLUX–FLUX CORRELATIONS

The luminosity–luminosity correlations might be caused, at least in part, by distance effects. Therefore, we also checked the correlations in flux–flux space. As expected, the correlations using the luminosities are stronger than the flux–flux correlations. However, they are still significant and we confirmed that the results presented in Section 6 hold in flux–flux space (see Table D1).

This paper has been typeset from a TEX/LATEX file prepared by the author.